INFORMING PREDICTIONS FROM ABOVE WITH DATA FROM BELOW: AN AI-DRIVEN SEISMIC GROUND-FAILURE MODEL FOR RAPID RESPONSE AND SCENARIO PLANNING

FINAL PROJECT REPORT

by

Brett W. Maurer
University of Washington

Sponsorship
PacTrans and WSDOT

for

Pacific Northwest Transportation Consortium (PacTrans)
USDOT University Transportation Center for Federal Region 10
University of Washington
More Hall 112, Box 352700
Seattle, WA 98195-2700

In cooperation with U.S. Department of Transportation,
Office of the Assistant Secretary for Research and Technology (OST-R)

DISCLAIMER

The contents of this report reflect the views of the authors, who are responsible for the facts and the accuracy of the information presented herein. This document is disseminated under the sponsorship of the U.S. Department of Transportation's University Transportation Centers Program, in the interest of information exchange. The Pacific Northwest Transportation Consortium, the U.S. Government and matching sponsor assume no liability for the contents or use thereof.

TECHNICAL REPORT DOCUMENTATION PAGE

1. Report No.	2. Government Accession No.	3. Recipient's Catalog No.
	01764504	

4. Title and Subtitle	5. Report Date
Informing Predictions from Above with Data from Below: An AI-Driven Seismic Ground Failure Model for Rapid Response and Scenario Planning	June 2022
	6. Performing Organization Code

7. Author(s) and Affiliations	8. Performing Organization Report No.
Brett W Maurer; 0000-0001-9305-5745 University of Washington	2020-S-UW-4

9. Performing Organization Name and Address	10. Work Unit No. (TRAIS)
PacTrans Pacific Northwest Transportation Consortium University Transportation Center for Federal Region 10 University of Washington More Hall 112 Seattle, WA 98195-2700	**11. Contract or Grant No.** 69A3551747110

12. Sponsoring Organization Name and Address	13. Type of Report and Period Covered
United States Department of Transportation Research and Innovative Technology Administration 1200 New Jersey Avenue, SE Washington, DC 20590	Single Institution
	14. Sponsoring Agency Code

15. Supplementary Notes

Report uploaded to: www.pactrans.org

16. Abstract

Geospatial models for predicting soil liquefaction infer subsurface traits via satellite remote sensing and mapped information, rather than directly measure them with subsurface tests. This project developed geospatial models that are driven by algorithmic learning but pinned to a physical framework, thereby benefiting from both machine and deep learning, or ML/DL, and the knowledge of liquefaction mechanics developed over the last 50 years. With this approach, subsurface cone penetration test (CPT) measurements are predicted remotely within the framing of a popular CPT model for predicting ground failure. This has three potential advantages: (i) a mechanistic underpinning; (ii) a significantly larger training set, with the model principally trained on in-situ test data, rather than on ground failures; and (iii) insights from ML/DL, with greater potential for geospatial data to be exploited. Models were trained using ML/DL and a modest U.S. dataset of CPTs to predict liquefaction-potential-index values via 12 geospatial variables. The models were tested on recent earthquakes and were shown—to a statistically significant degree—to perform as well as, or better than, the current leading geospatial model. The models are coded in free, simple-to-use Windows software. The only input is a ground-motion raster, downloadable minutes after an earthquake or available for countless future scenarios. To demonstrate model use, ground failure probabilities were computed for 30 ground-motion simulations of a magnitude 9, Cascadia Subduction Zone earthquake, at every bridge site in Washington state. These analyses, as further detailed and mapped herein, indicated that: 13 bridges had at least a 70 percent probability of ground failure; 218 bridges had at least a 60 percent probability of ground failure; and 795 bridges had at least a 50 percent probability of ground failure. These analyses did not consider specific asset designs or site-specific ground improvements. The analyses did, however, provide a ranked list of bridge sites most likely to be damaged by ground failure. Select ground-truthing lent credence to the developed models and results.

17. Key Words	18. Distribution Statement
Earthquake; liquefaction; emergency management	

19. Security Classification (of this report)	20. Security Classification (of this page)	21. No. of Pages	22. Price
Unclassified.	Unclassified.	54	N/A

Form DOT F 1700.7 (8-72) **Reproduction of completed page authorized.**

SI* (MODERN METRIC) CONVERSION FACTORS

APPROXIMATE CONVERSIONS TO SI UNITS				
Symbol	**When You Know**	**Multiply By**	**To Find**	**Symbol**
		LENGTH		
in	inches	25.4	millimeters	mm
ft	feet	0.305	meters	m
yd	yards	0.914	meters	m
mi	miles	1.61	kilometers	km
		AREA		
in^2	square inches	645.2	square millimeters	mm^2
ft^2	square feet	0.093	square meters	m^2
yd^2	square yard	0.836	square meters	m^2
ac	acres	0.405	hectares	ha
mi^2	square miles	2.59	square kilometers	km^2
		VOLUME		
fl oz	fluid ounces	29.57	milliliters	mL
gal	gallons	3.785	liters	L
ft^3	cubic feet	0.028	cubic meters	m^3
yd^3	cubic yards	0.765	cubic meters	m^3
	NOTE: volumes greater than 1000 L shall be shown in m^3			
		MASS		
oz	ounces	28.35	grams	g
lb	pounds	0.454	kilograms	kg
T	short tons (2000 lb)	0.907	megagrams (or "metric ton")	Mg (or "t")
		TEMPERATURE (exact degrees)		
°F	Fahrenheit	5 (F-32)/9 or (F-32)/1.8	Celsius	°C
		ILLUMINATION		
fc	foot-candles	10.76	lux	lx
fl	foot-Lamberts	3.426	$candela/m^2$	cd/m^2
		FORCE and PRESSURE or STRESS		
lbf	poundforce	4.45	newtons	N
lbf/in^2	poundforce per square inch	6.89	kilopascals	kPa

APPROXIMATE CONVERSIONS FROM SI UNITS				
Symbol	**When You Know**	**Multiply By**	**To Find**	**Symbol**
		LENGTH		
mm	millimeters	0.039	inches	in
m	meters	3.28	feet	ft
m	meters	1.09	yards	yd
km	kilometers	0.621	miles	mi
		AREA		
mm^2	square millimeters	0.0016	square inches	in^2
m^2	square meters	10.764	square feet	ft^2
m^2	square meters	1.195	square yards	yd^2
ha	hectares	2.47	acres	ac
km^2	square kilometers	0.386	square miles	mi^2
		VOLUME		
mL	milliliters	0.034	fluid ounces	fl oz
L	liters	0.264	gallons	gal
m^3	cubic meters	35.314	cubic feet	ft^3
m^3	cubic meters	1.307	cubic yards	yd^3
		MASS		
g	grams	0.035	ounces	oz
kg	kilograms	2.202	pounds	lb
Mg (or "t")	megagrams (or "metric ton")	1.103	short tons (2000 lb)	T
		TEMPERATURE (exact degrees)		
°C	Celsius	1.8C+32	Fahrenheit	°F
		ILLUMINATION		
lx	lux	0.0929	foot-candles	fc
cd/m^2	$candela/m^2$	0.2919	foot-Lamberts	fl
		FORCE and PRESSURE or STRESS		
N	newtons	0.225	poundforce	lbf
kPa	kilopascals	0.145	poundforce per square inch	lbf/in^2

*SI is the symbol for the International System of Units. Appropriate rounding should be made to comply with Section 4 of ASTM E380.
(Revised March 2003)

TABLE OF CONTENTS

LIST OF FIGURES

LIST OF TABLES

EXECUTIVE SUMMARY

Geospatial models for predicting soil liquefaction infer subsurface traits via satellite remote sensing and mapped information, rather than directly measure them with subsurface tests. Field tests of such models have demonstrated both promising potential and severe shortcomings. Informed by these tests, this study developed geospatial models that are driven by algorithmic learning but pinned to a physical framework, thereby benefiting from both machine and deep learning, or ML/DL, and the knowledge of liquefaction mechanics developed over the last 50 years. With this approach, subsurface cone penetration test (CPT) measurements are predicted remotely within the framing of a popular CPT model for predicting ground failure. This has three potential advantages: (i) a mechanistic underpinning; (ii) a significantly larger training set, with the model principally trained on in-situ test data, rather than on ground failures; and (iii) insights from ML/DL, with greater potential for geospatial data to be exploited.

While liquefaction is a phenomenon best predicted by mechanics, subsurface traits lack theoretical links to above-ground parameters but correlate in complex, interconnected ways—a prime problem for ML/DL. Preliminary models were trained using ML/DL and a modest U.S. dataset of CPTs to predict liquefaction-potential-index values via 12 geospatial variables. The models were tested on recent earthquakes and were shown—to a statistically significant degree—to perform as well as, or better than, the current leading geospatial model. The models are coded in free, simple-to-use Windows software. The only input is a ground-motion raster, downloadable minutes after an earthquake or available for countless future scenarios. This gives the product near-real-time capabilities, such that ground failure may be predicted across the PacTrans Region 10 (e.g., the State of Washington) minutes after an event.

Ultimately, the proposed approach and models, which warrant further application and evaluation, could be improved upon using additional training data and new predictor variables. Users of the models should understand key limitations, as discussed in detail herein. To demonstrate application to transportation networks, ground failure probabilities, considering 30 ground-motion simulations of a magnitude 9, Cascadia Subduction Zone earthquake, were computed for 5,020 Washington state bridges in the National Bridge Inventory. These analyses, as detailed and mapped herein, indicated that of the 5,020 bridges: (i) 13 bridges had at least a 70 percent probability of ground failure; (ii) 218 bridges had at least a 60 percent probability of ground failure; and (iii) 795 bridges had at least a 50 percent probability of ground failure. These

analyses did not consider specific asset designs or site-specific ground improvement works that may or may not have been carried out. The analyses did, however, provide a ranked list of bridge sites most likely to be damaged by ground failure. Select ground-truthing lent credence to the developed models and predictions. These predictions may be further investigated (e.g., via network analyses) to identify critical corridors likely to experience outages and/or to prioritize bridges for more advanced studies and possible earthquake retrofitting.

The models resulting from this project thus allow liquefaction-induced ground failure to be predicted rapidly, remotely, and at regional scale, either in advance of an event for planning and mitigation, or minutes after an event for response and recovery.

CHAPTER 1. INTRODUCTION

As evidenced by earthquakes occurring globally each year, reliable predictions of soil liquefaction are needed both before an earthquake for efficient planning and mitigation and immediately after an earthquake for informing response, reconnaissance, and recovery. Such predictions would thus ideally have the capability of being made (i) rapidly (e.g., in near-real-time after an event); (ii) at high resolution (e.g., consistent with the scale of individual assets); and (iii) over the regional extents impacted by large earthquakes (e.g., that of a metropolis or transportation system). Problematically, state-of-practice liquefaction models require relatively costly geotechnical data, such as that from the cone penetration test (CPT). Given the infeasibility of in-situ testing across vast areas, regional-scale predictions of liquefaction (e.g., at regionally distributed bridge locations) have traditionally relied on geologic maps, from which generic classifications of liquefaction susceptibility may be assumed (e.g., Youd and Hoose, 1977). Such an approach is simple but also unacceptably uncertain for most intents.

Alternatively, statistical distributions of geotechnical data within geologic units may be developed and used to predict liquefaction (e.g., Holzer et al., 2011). This is more data-driven and likely to be more accurate, but many in-situ tests are still required within each mapped unit of interest. Moreover, predictions using this approach have the coarse resolution of geologic maps and assume intra-unit uniformity (i.e., local conditions are not considered), meaning an entire city could potentially receive the same prediction. It thus remains a persistent challenge to model liquefaction (or any geohazard) in a manner that is regional and rapid, yet high resolution and accurate. The existence of a model having these traits is conceivable, however, given the growth of community geotechnical datasets, remote sensing, and algorithmic learning (i.e., machine and deep-learning, or ML/ML).

Toward that end, interest has grown in prediction models that use inputs readily available from satellite remote-sensing and existing, mapped information. In contrast to geotechnical methods, “geospatial” models can predict liquefaction rapidly, at infinitely many locations. This is made possible using geospatial proxies of soil properties relevant to liquefaction (i.e., above-ground inferences of below-ground conditions). While the concept of such a model is not new (e.g., Kramer, 2008; FEMA, 2013), the model of Zhu et al. (2017), lightly modified by Rashidian and Baise (2020), is arguably the most rigorously formulated and widely accepted. It is also implemented in the United States Geological Survey (USGS) “PAGER” system, which provides

content on possible earthquake impacts (Wald et al., 2008). In a recent study, Geyin et al. (2020) tested the Zhu et al. (2017) model against 18 CPT-based models using ~15,000 liquefaction case histories (essentially all CPT-based case histories globally available to date). These analyses elucidated the provocative potential of geospatial data, as well as significant room, and potential means, for improving existing geospatial models. Informed by these analyses, this study aimed to develop an improved geospatial model driven by algorithmic learning (benefiting from ML/DL insights) but pinned to a physical framework (benefiting from mechanics and the knowledge of regression modelers). In the following, the typology of liquefaction models is succinctly summarized (to place this project, and the methods it utilized, in context). Next, tests of the Zhu et al. (2017) model are summarized and lessons for improvement are discussed, as are the advantages of the proposed approach. This approach was then used to develop three ML/DL models that predict the probability of liquefaction-induced ground failure. Finally, these models were tested using unbiased data and implemented in *RapidLiq*, a new Windows software program.

1.1. A Succinct Overview of Geotechnical and Geospatial Liquefaction Models

The typology of models for predicting liquefaction roughly consists of three tiers: (Tier 1) fully-empirical models that require only geospatial or geologic information (e.g., Rashidian and Baise, 2020); (Tier 2) semi-mechanistic "stress-based" models that require in-situ test data and are widely used in engineering practice (e.g., Boulanger and Idriss, 2014; Green et al., 2019); and (Tier 3) numerical constitutive models, which require many material and model parameters (e.g., Cubrinovski and Ishihara, 1998; Ziotopoulou and Boulanger, 2016). While improvements to computational throughput have grown the use of "Tier 3" models, their application is still limited to specific sites and special projects, given the required inputs and operator skill. Given the rapid and regional scale aims of the proposed work, "Tier 3" models will not be used herein, which is not to say that such models could not conceivably be implemented at regional scale.

Many "Tier 2" models are popular in engineering practice. These include, among others, Robertson and Wride (1998), Moss et al. (2006), Idriss and Boulanger (2008), Boulanger and Idriss (2014), and Green et al. (2019), which all use data from the CPT to predict liquefaction as a function of earthquake magnitude (M_w) and peak ground acceleration (PGA). However, because these models predict the factor of safety against liquefaction "triggering" (FS_{liq}) at-depth within a profile, the outputs are often used cooperatively with other models that predict manifestations of

liquefaction at the surface (i.e., "ground failure"). One popular manifestation model is the liquefaction potential index (*LPI*), proposed by Iwasaki et al. (1978):

$$LPI = \int_0^{20\ m} F(FS_{liq}) \cdot w(z)\ \mathrm{d}z \qquad \text{(Eq 1)}$$

where $F(FS_{liq})$ and $w(z)$ weight the respective influences of FS_{liq} and depth, z, on surface manifestation. Specifically, $F(FS_{liq}) = 1 - FS_{liq}$ for $FS_{liq} \leq 1$ and $F(FS_{liq}) = 0$; otherwise, $w(z) = 10 - 0.5z$. *LPI* thus assumes that surface manifestation depends on the thickness of all liquefied strata in the upper 20 m, the degree to which FS_{liq} in each stratum is less than 1.0, and how near those strata are to the surface. *LPI* can range from zero to 100, with surface manifestations becoming more likely as *LPI* increases (e.g., Maurer et al., 2014; Geyin and Maurer, 2020a). Other similar manifestation models include those of van Ballegooy et al. (2014) and Maurer et al. (2015a).

"Tier 1" geospatial models, which aim to predict liquefaction via readily available predictor variables, have recently received renewed attention. Like "Tier 2" models, geospatial models characterize liquefaction demand via ground-motion intensity measures (IMs) (e.g., *PGA*). But, instead of quantifying liquefaction resistance with in-situ measurements, geospatial models predict below-ground conditions using above-ground information. Examples of such predictors include (among many) the slope and roughness of the surface; the distance to rivers and coasts; and compound-topographic-index, which can be derived from satellite data or existing prediction maps. Geospatial models are well suited for regional scale applications such as (i) loss estimation and disaster simulation; (ii) city planning and policy development; (iii) emergency response; and (iv) post-event reconnaissance (e.g., to remotely identify sites of interest).

The geospatial model originally proposed by Zhu et al. (2017) is a logistic regression model of the form $P(X) = (1 + e^{-X})^{-1}$ where X is a sequence of predictor variables and coefficients, and $P(X)$ is the likelihood of ground failure (i.e., surface manifestation). The model, which was trained on observations of ground-failure, takes on two forms depending on a site's vicinity to a coastline. The equations for model parameter X are in table 1.1. The variables are PGV = peak ground velocity (cm/s); V_{S30} = shear-wave velocity of the upper 30-m (m/s) predicted from topography (Wald and Allen, 2007); *dr* = closest distance to a river (km) in the Lehner et al. (2006) dataset; *dc* = distance to coast (km); *dw* = the lesser of *dr* and *dc* (km); *precip* = mean annual precipitation (mm) (Fick and Hijmans, 2017); and *wtd* = predicted water table depth (m) (Fan and Miguez-Macho, 2013). Following additional testing, Rashidian and Baise (2020) proposed two minor

modifications to mitigate false positive predictions: (i) the model's output should be reassigned as zero below a *PGA* of 0.1 g; and (ii) the *precip* input should be capped at 1700 mm/yr.

Table 1.1 Geospatial model equations (Zhu et al., 2017; Rashidian and Baise, 2020)

Model	Model Parameter X
(Coastal)	$12.435 + 0.301 \cdot \ln(PGV) - 2.615 \cdot \ln(V_{s30}) + 5.556 \times 10^{-4} \cdot precip - 0.0287 \cdot (d_c)^{0.5} + 0.0666 \cdot d_r - 0.0369 \cdot d_r \cdot (d_c)^{0.5}$
(Inland)	$8.801 + 0.334 \cdot \ln(PGV) - 1.918 \cdot \ln(V_{s30}) + 5.408 \times 10^{-4} \cdot precip - 0.2054 \cdot d_w - 0.0333 \cdot wtd$

1.2. A Test of Geospatial Liquefaction-Model Performance

Using approximately 15,000 liquefaction case histories compiled from 23 earthquakes by Geyin et al. (2021) and Geyin and Maurer (2021a), Geyin et al. (2020) tested the Zhu et al. (2017) geospatial model against 18 different CPT methods for predicting liquefaction surface manifestation. These comprised six different triggering models used in series with three different manifestation models. Because most of the case histories were sourced from three events in Canterbury, New Zealand, test cases were parsed into the "Canterbury" and "Global" datasets. Performance was quantified via receiver-operating-characteristic (ROC) analyses – specifically the area under the ROC curve, or *AUC*—which is a popular metric of prediction efficiency (e.g., Fawcett, 2006). Using this metric, a perfectly efficient model achieves an *AUC* of 1.0, whereas a model on par with random guessing achieves an *AUC* of 0.5. ROC analyses are also attractive in that they are insensitive to changes in class distribution. If the proportion of negative to positive instances in a test set changes, the *AUC* results will not change (Fawcett, 2006). P-values were computed per the method of DeLong et al. (1988) to determine whether measured differences in *AUC* could have arisen by chance (i.e., due to finite-sample uncertainty) and not because one model was more efficient than another.

While the reader is referred to Geyin et al. (2020) for complete details, the most salient results are summarized as follows. First, on the "Canterbury" dataset, the geospatial model performed significantly better than 16 out of 18 CPT models, with a measured *AUC* of 0.84. Against the top two CPT models, it was statistically indifferent, and thus either outperformed or matched all 18 CPT models. This was a surprising result, given the relative costs of the required model inputs. Second, on the "Global" dataset, all geotechnical models performed significantly better than the Zhu et al. (2017) model, with the latter performing only somewhat better than

random guessing with an AUC of 0.55. This might be expected, given (i) the variation of geomorphic, topographic, and climatic environs in a global dataset; and (ii) the challenge, given this variation, of accurately predicting below-ground conditions from above-ground parameters. Inherently, the CPT models—being based on subsurface tests—*should* be more portable across environments. Nonetheless, the strong performance of the seminal Zhu et al. (2017) model in Canterbury demonstrated the promising potential of geospatial data for regional-scale purposes, a conclusion similarly reached by Lin et al. (2021b).

1.3. Limitations of Existing Geospatial Modelling Approaches

By way of the study above, possible shortcomings of the Zhu et al. (2017) and Rashidian and Baise (2020) geospatial model, henceforth referred to as RB20, were identified. It should be emphasized that this model transformed the perception of geospatial modeling for geohazards. Nonetheless, like all models, it has shortcomings that could be improved upon.

First, RB20 was trained directly on outcomes (i.e., observations of ground failure) rather than on the mechanistic causes of those outcomes (i.e., subsurface engineering properties). While this lack of a mechanistic underpinning can be overcome with vast training data (e.g., how voice transcription apps predict words without understanding language), current ground failure inventories are arguably too sparse. Specifically, both "positive" and "negative" cases (i.e., sites with and without observed liquefaction) are needed in which predictor variables span the range of possible values. That is, the parameter space of all predictor variables should be fully populated. Yet, while liquefaction is common in earthquakes, ground failure inventories are slow to grow (relative, for example, to those of in-situ test data). Given the adopted approach, inadequate training data can result in a divergence from mechanistic principles (e.g., prediction of liquefaction given shaking too weak, from a mechanistic perspective, to induce liquefaction).

Second, RB20 uses just five variables. Four represent capacity (distance to surface water; precipitation; and mapped V_{S30} and groundwater depth) and one represents demand (PGV). Notably, none of these variables is likely to correlate to the type of soil, or by corollary, to the susceptibility of the soil to liquefaction. This was a common cause of mispredictions identified in the Geyin et al. (2020) study, with RB20 expecting susceptibility if the ground is flat, saturated, and near water. However, such profiles can consist mostly of soils less- or un-susceptible to liquefaction (e.g., clays, peats, or gravels). Moreover, we find in many such cases that geologic maps accurately

predict the presence of such soils. An improved model might thus use mapped geologic data, when available, and/or other yet unidentified proxies of soil type.

Third, and following from the above, RB20 is a traditional regression equation. This method of modeling inherently requires hypotheses of what is believed to matter and how (beliefs that are unnecessary with ML/DL). The efficient prediction of subsurface traits likely requires more than four geospatial variables, yet regression limits the number easily modeled. Algorithmic learning would allow more geospatial predictor variables to be used, with greater potential for those variables/data to be exploited fully.

1.4. The Proposed Modelling Approach and its Potential Benefits

This project proposed a new geospatial modeling approach that is driven by algorithmic learning but pinned to an established mechanistic framework. Specifically, ML/DL models would be trained to predict *LPI* values in the absence of subsurface test data. Before model training, *LPI* values would be computed from a national database of in-situ geotechnical tests subjected to a range of hypothetical ground motions. During model training, the ML/DL models would learn to predict these *LPI* values using 12 predictor variables. These variables would consist of *PGA* and M_w, which are "demand" variables, and ten geospatial parameters from the geotechnical test site, which are "capacity" variables. The goal of these ten geospatial variables, in effect, would be to predict the relationship between *LPI* and seismic loading in the absence of subsurface data. Multiple models would be developed and ensembled, thereby avoiding large "swings" on account of which model was chosen (as is common in prediction of ground motions, hurricane tracks, etc.). When used in the forward direction, the trained models would predict *LPI* at sites without geotechnical testing, given *PGA*, M_w, and geospatial variables sampled at the coordinates of the sites. To complete the prediction of ground failure, the predicted *LPI* values would be input to existing fragility functions (Geyin and Maurer, 2020a) that predict the probability of liquefaction manifestation (i.e., "ground failure") as a function of *LPI*. These functions would be trained on a large database of well-documented liquefaction case histories compiled from 24 global earthquakes. Thus, the ultimate output would be a predicted probability of ground failure (the same as RB20). A synopsis of the proposed approach is shown in figure 1.1.

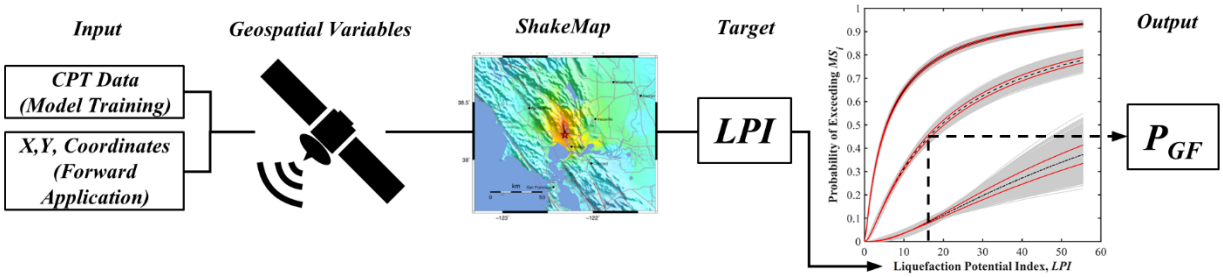

Figure 1.1 Synopsis of the approach to predicting probability of ground failure (PGF)

This approach had several potential advantages.

First, the principal prediction target was transferred from ground failure (with relatively sparse training data) to subsurface measurements (for which the potential training set was vast). Because the location of in-situ tests need not have experienced an earthquake (i.e., be a liquefaction case history), significantly more training data were available. Given the rise of community geotechnical datasets—both internationally and in the U.S.—the gap between the number of subsurface tests and the number of liquefaction case histories will likely grow. We hypothesized that this larger training set would be advantageous, both now and in the future.

Second, liquefaction is a physical phenomenon best predicted by mechanics. Much has been learned about liquefaction over the last 50 years. This knowledge is embedded in current state-of-practice liquefaction triggering and manifestation models. We hypothesized that anchoring to these models, which provide a mechanistic foundation, would be advantageous, given their validated ability to model liquefaction response as a function of soil and profile traits (e.g., subsurface stratigraphy, soil density, fines-content, plasticity, saturation, ground motion duration and intensity).

Third, whereas liquefaction is best predicted by mechanics, subsurface traits lack theoretical links to above-ground parameters (i.e., geospatial data), but surely correlate to them in complex, interconnected ways. This is a prime problem for ML/DL, which can provide learning insights that are simply unlikely, if not altogether infeasible, with regression approaches. We hypothesized that ML/DL would provide the potential for geospatial data to be exploited more fully.

Fourth, the models could be updated relatively easily as additional training data (in-situ tests) become available. In the short term, some geospatial variables could be viewed by the learning algorithms as relatively unimportant, either because they truly were unimportant or because there was insufficient training data to elucidate their predictive value. The RB20 model for

predicting ground-failure is also retrainable, but we hypothesized that meaningful growth in the ground-failure dataset would take place at a slower pace (e.g., with data from a few events annually that impact a small fraction of Earth).

CHAPTER 2. MODEL DATA AND METHODOLOGY

In the current effort, two models were developed using relatively modest sets of training data and predictor variables compiled in the United States (U.S.). As will be discussed, the proposed approach could be extended by using additional training data and new predictor variables at regional, national, or global scales. Nonetheless, the developed models, which are applicable to the U.S., were shown to be at least as efficient as other geospatial models and thus warrant application and further evaluation, even if preliminary in nature.

While several in-situ geotechnical tests could be used within the proposed approach, we chose CPT data, given that (i) it has inherent advantages over other tests upon which liquefaction models have been based (NRC, 2016); (ii) the Geyin and Maurer (2020a) fragility functions were trained on CPT-based case histories; and (iii) a U.S. national CPT database is readily available in native digital format. Specifically, the USGS national database of 1,712 CPTs (USGS, 2021) was adopted for analysis. This dataset provided somewhat well-distributed measurements, as mapped in figure 2.1, in a range of environments, generally in high-seismicity regions. Approximately 5 percent were from sites where liquefaction case histories were compiled following modern earthquakes. Given the limited dataset, some regions of the U.S. were unrepresented in model development, as shown in figure 2.1. Ultimately, however, tests of the derivative geospatial models were not clearly suggestive of regional bias (i.e., the models performed well in regions with no training data). Nevertheless, it stands to reason that an expanded dataset would result in better models. Of the 1,712 CPTs, 20 percent were randomly selected and reserved for model testing, while the remaining 80 percent were used for model training.

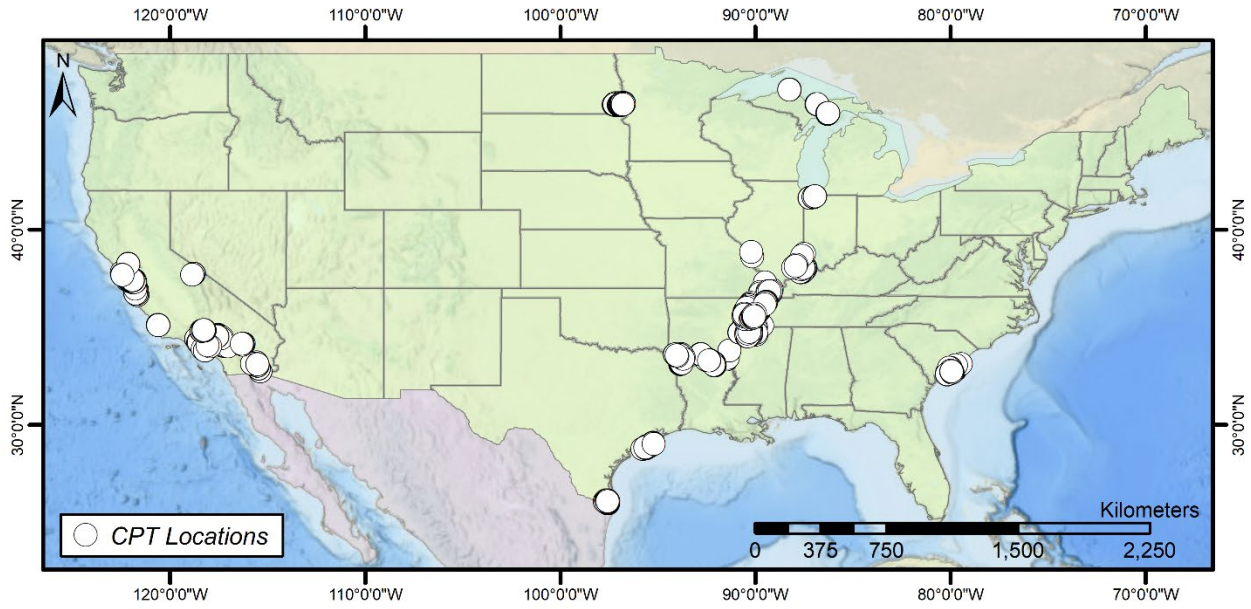

Figure 2.1 Spatial distribution of CPT training and test data

Next, each CPT was subjected to 152 combinations of *PGA* and M_w, with *PGA* ranging from 0.0 g to 1.0 g and M_w ranging from 4.5 to 9.0. These represented loadings that could hypothetically impact a site and for which it would be of interest to predict liquefaction. We excluded $M_w < 4.5$ events based on Green and Bommer (2019). With the proposed approach, however, it was irrelevant whether the CPT sites ever experienced an earthquake or whether a specific combination of *PGA* and M_w could feasibly occur in the future. In other words, we assumed that subsurface conditions were generally independent of the seismic hazard (i.e., saturated, loose, cohesionless soils are equally present in high seismicity regions as in low seismicity regions). As such, it was not necessary that CPTs be subjected to site-specific combinations of *PGA* and M_w that were more likely to occur (e.g., according to a probabilistic seismic hazard analysis). For each combination of *PGA* and M_w, the Idriss and Boulanger (2008) CPT liquefaction model was used to predict FS_{liq} versus depth. These predictions were then input to the *LPI* manifestation model, as defined in Equation. 1. All CPT processing and calculations were performed using the software *Horizon* (Geyin and Maurer, 2020b). While different, or additional, triggering and/or manifestation models could be used, the Idriss and Boulanger (2008) triggering model—when used in conjunction with *LPI*—demonstrated an efficiency that was never bested, to a statistically significant degree, by any other model when tested on global case-history data (Geyin et al., 2020). In addition, the magnitude-scaling factor (*MSF*) inherent to Idriss and Boulanger (2008) was soil-independent,

whereas other triggering models (Boulanger and Idriss, 2014; Green et al., 2019) had *MSF*s that varied with depth depending on the inferred relative density. The more predictable scaling of computed *LPI* with increasing M_w was deemed advantageous for modeling, given the limited training data utilized herein. A subsequent study could explore the use of other CPT models, although previous testing of such models (Geyin et al., 2020) suggested that the efficacy of the resulting product would be very similar.

Given the 1,712 CPTs and 152 combinations of seismic loading, a total of 260,224 *LPI* values were computed. These values are plotted in figure 2.2 as a function of magnitude-scaled *PGA* ($PGA_{M7.5}$), as computed by Idriss and Boulanger (2008), and they formed the primary prediction target of the proposed modeling approach. At sites of high liquefaction hazard (i.e., thick deposits of saturated, loose sand), *LPI* increased rapidly with $PGA_{M7.5}$, whereas at sites of low hazard (i.e., sites devoid of soil susceptible to liquefaction), *LPI* could remain near zero for all $PGA_{M7.5}$. The goal of the geospatial modeling, in effect, was to predict the relationship between *LPI* and seismic loading (*PGA*, M_w) in the absence of subsurface data.

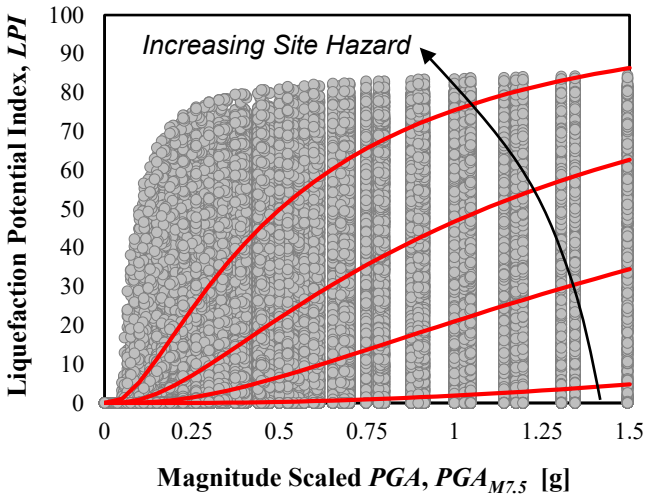

Figure 2.2 *LPI* versus $PGA_{M7.5}$; plotted are 260,224 *LPI* values computed from 1,712 CPTs subjected to 152 different levels of seismic loading

Ten geospatial predictor variables were next compiled at the coordinates of each CPT. The goal of these ten variables was to correlate to the subsurface conditions that give rise to low or high *LPI*. These consisted of predicted V_{S30} (Heath et al., 2020); predicted ground water depth (Fan and Miguez-Macho, 2020); measured distance to a river (Lehner et al., 2006) and measured distance to the coast (NASA, 2012); predicted depth to bedrock (Shangguan et al. 2017); measured annual

precipitation (Fick and Hijmans, 2017); and the predicted (binomial) presence of unconsolidated soil, sandy soil, clayey soil, and silty soil, as obtained from the USGS National Geologic Map compilation (Horton et al. 2017). The intention of the latter four variables was to predict whether soil was present, and if so, whether it had one of these three predominant soil types. Additional mapped soil types were ultimately found not to be useful, as will be further discussed. The range of predictor variables in the dataset and their spatial resolutions are given in table 2.1.

Table 2.1 Range of predictor variables in the dataset and their spatial resolutions

Variable (Units)	**Range in Dataset**	**Spatial Resolution**
Earthquake Magnitude (M_w)	4.5 to 9	N/A
Peak Ground Acceleration (g)	0 to 1	N/A
Ground Water Table Depth (m)	0 to 216	~1000 m (30 arc-sec)
Distance to River (m)	2 to 6,220	~90 m (3 arc-sec)
Distance to Coastline (km)	0 to 1,210	~90 m (3 arc-sec)
Depth to Bedrock (cm)	379 to 21,717	250 m
Annual Precipitation (mm)	68 to 1,389	~1000 m (30 arc-sec)
V_{S30} (m/s)	92 to 713	~1000 m (30 arc-sec)
Unconsolidated Soil (binomial)	0 or 1	25 m to 500 m (varies)
Dominant Clay (binomial)	0 or 1	
Dominant Silt (binomial)	0 or 1	
Dominant Sand (binomial)	0 or 1	

In lieu of predicted V_{S30}, we also explored the use of measured topographic slope, which ultimately produced models with nearly identical performance. This was unsurprising, given that V_{S30} was most often predicted solely from topographic slope in the Heath et al. (2020) compilation, which merged several regional V_{S30} maps with a general slope-based V_{S30} model. However, we adopted the predicted V_{S30} from Heath et al. (2020), given that it included region-specific insights into the relationship between topographic slope and subsurface conditions. While the potential benefits of using V_{S30} from Heath et al. (2020) (i.e., versus topographic slope) were not realized

during model training and testing, such benefits could conceivably be observed in future, forward applications elsewhere. Notably, models developed without either parameter performed significantly worse. The importance of each predictor variable will be further discussed later in the paper.

Using the training set (80 percent of CPTs), models were next developed to remotely predict *LPI* as a function of *PGA* and M_w, which could be viewed as "demand" variables, and of the ten geospatial variables, which could be viewed as "capacity" variables. The latter could be compiled at national scale in advance of model application. The former are available at regional scale minutes after an earthquake (e.g., via a single "ShakeMap" file (Wald et al., 2005)) or for various future earthquake scenarios. Like other geospatial models, this gives the model near-real-time functionality, such that ground failure could be predicted at regional scale minutes after an event. Various ML/DL techniques were explored, including Gaussian process models (e.g., Rasmussen and Williams, 2006); support vector machines (SVM) (e.g., Vapnik, 1995); decision trees (e.g., Rokach and Maimon, 2008); model ensembles with bagging, gradient boosting, or random forests (e.g., Breiman, 1996; Piryonesi et al., 2021; Ho, 1998); and neural networks (e.g., Glorot et al., 2010). In general, modeling approaches that are easier to interpret tend to have lower predictive accuracy (e.g., single decision trees, support vector machines), while those with higher accuracy (e.g., neural networks or ensembles of decision trees) are typically very complex to interpret. Each approach has numerous options and internal parameters (i.e., "hyperparameters") (e.g., neural net optimization algorithm, activation function, and layer quantity and size; regression tree leaf size; Gaussian basis and kernel functions; SVM kernel scale and box constraint).

Once promising models had been identified, hyperparameter optimization was employed, such that the hyperparameter values that minimized the model error were identified via an automated optimization scheme. five-fold cross-validation was used to control overfitting, as is common in model development. Additionally, training and test performance metrics were compared for signs of overfitting (i.e., better training performance than test performance), which was inferred when performance metrics from the training and test sets differed by at least 4 percent. In this regard, models with slightly lower accuracy but without overfitting were favored over models that achieved the highest training accuracy but with suspicion of overfitting. Because many ML/DL algorithms either require or perform better when variables have a Gaussian distribution, all predictors were BoxCox transformed (Box and Cox, 1964) and normalized to have values of

between 0 and 1. Ultimately, the software in which the prediction models were implemented performed all necessary computations, and as such, no pre-processing of data were required (e.g., predictor variables were input in their native format).

CHAPTER 3. MODEL RESULTS AND DISCUSSION

Using the aforementioned methodology with relatively modest sets of training data and predictor variables, several dozen preliminary models were trained. Of these, two were ultimately adopted for further implementation and testing. The first model adopted was a boosted ensemble of decision trees, wherein numerous relatively weak models are coalesced to form one high-quality model. For brevity, we henceforth refer to it as the "ML model." The theory and algorithm underlying this approach – which is commonly included in machine learning toolkits (e.g., Scipy, TensorFlow)—was explained in detail by Friedman (2001). An excellent overview of its practical implementation was provided by Elith et al. (2008). The growth of a decision tree involves establishment of recursive binary splits, such that specific combinations of model inputs map to a predicted output. However, because a single tree is prone to overfitting and tends not to be very accurate, models that ensemble many decision trees are preferred. In "gradient boosting," a strong learner is sequentially built from weak learners, wherein each tree attempts to diminish the errors of the previous tree by gradually increasing emphasis on observations poorly predicted by the ensemble. While gradient boosting is slow, it generally produces a more accurate model than other assembling algorithms (e.g., bagging or random forests) (Piryonesi et al., 2021). With respect to performance, the ML model achieved a mean absolute error (MAE) (*LPI* units) of 3.58 and 3.72 on the training and test sets, respectively, as summarized in table 3.1. As discussed previously, the unbiased test set consisted of *LPI* data from CPT sites unknown to the model during training.

The second adopted model was a deep (seven-layer) artificial neural network, which we henceforth refer to as the "DL model." With roots in the 1980s (e.g., Hopfield, 1982), this now ubiquitous approach mimics the perceived structure of the human brain, with layers of interconnected nodes. At the most basic level, DL models have four components: inputs, weights, a threshold, and an output. Connections between nodes are modelled as weights, such that positive and negative weights indicate excitatory and inhibitory connections, respectively. If the output from an individual node is above a specified threshold, the node is activated, sending data to the next layer of the network. An activation function then controls the amplitude of the output at each node. As DL models have multiple layers, the above process is repeated multiple times, with each layer potentially passing information from the previous layer to the next. During training, the weights are iteratively adjusted to optimize model performance. Like the ML model, DL models are quite convoluted, rendering simple interpretations of the inner workings infeasible, since single node

weights have little physical meaning, and since millions of connections may be present in a model. As shown in table 3.1, the DL model achieved an MAE of 4.13 and 4.20 on the same respective datasets (i.e., it performed slightly worse than the ML model). Given the limited training set and preliminary nature of the ML and DL models, we also created a third “Ensemble model" by averaging the outputs of the ML and DL models. The merging of two models with different structures could have the effect of “stabilizing” predictions and, conceivably, provide benefits unrealized during testing. As shown in table 3.1, the ensemble performed better than the DL model and worse than the ML model, although all were similarly efficient when considering the range of the *LPI* domain (i.e., zero to 100). The performance of these models, and other results in table 3.1, will be further discussed momentarily.

Table 3.1 Summary of model performance (mean absolute error) on the training, test, and overall datasets

Model	Mean Absolute Error (*LPI* Units)			Mean Absolute Error (Probability Units)		
	Training	Test	Overall	Training	Test	Overall
ML	3.5814	3.7237	3.6642	7.1691	7.6482	7.3698
DL	4.1329	4.2097	4.175	8.6918	8.9609	8.7894
Ensemble	3.743	3.8499	3.8039	7.6491	8.0338	7.7967

While the convoluted nature of ML/DL models tends to obscure simple interpretations of model function (e.g., relative to traditional regression), insights into the ML decision-tree ensemble can be gained via predictor importance (e.g., Auret and Aldrich, 2011), which may be interpreted as the relative contribution of each variable to model accuracy. Accordingly, the relative importance of each variable was computed, and it is plotted in figure 3.1, where variables are sorted from most to least important. This approach and presentation mirrors that of Durante and Rathje (2021), who explored the ML prediction of lateral spreads using geospatial data. As could be expected, the magnitude-scaled *PGA* and predicted groundwater depth had the largest importance, given the mechanistic relationship between these inputs and computed *LPI*. Also of relatively large importance were the measured distance to a river and predicted depth to the bedrock, which correlated to the expected thickness and geomorphology of deposits. Bedrock at shallow depth limits *LPI* ,while bedrock at very large depth suggests the presence of a sedimentary basin, which tends to collect sands and silts in a low-velocity flow regime. The presence of a nearby river, particularly in combination with flat topography, suggests a similar geomorphology, while also

indicating that the deposits are likely young and saturated. Of the compiled geologic data, the predicted predominance of clay was most important, whereas the predicted predominance of silt was least important. This aligned with expectations, given the established use of the plasticity index to infer liquefaction susceptibility within mechanistic models. Whereas soils classified as clay are rarely susceptible, silts are an intermediate soil whose liquefaction response is difficult to predict from name alone. We hypothesize that the overall importance of mapped soil type could increase if the set of training sites were larger and more diverse, given that the set used herein did not span the full range of geologic conditions that may be encountered. While the computed predictor importance gives insights into decision-tree models, we are unaware of any analogous tool for studying neural networks, which thus remain relatively more convoluted.

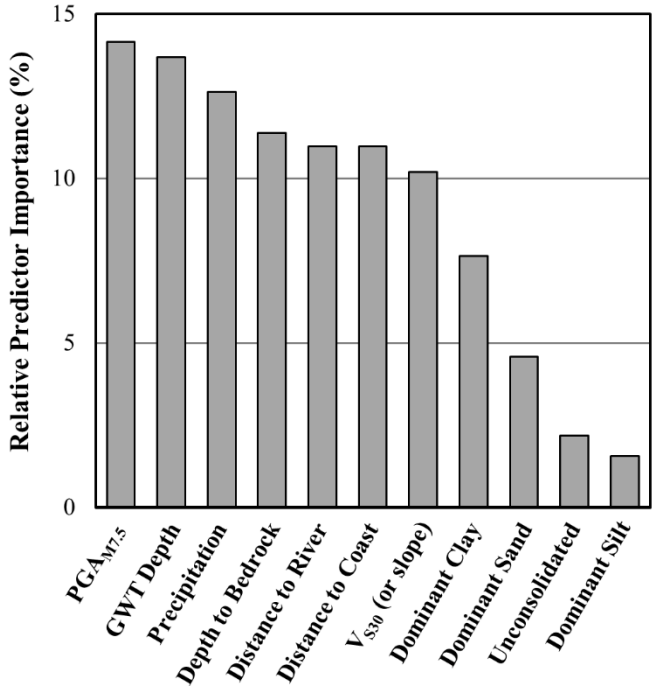

Figure 3.1 Relative predictor importance ranking for the ML model

Following prediction of *LPI* via the ML, DL, or Ensemble models, probabilities of ground failure were computed using the Geyin and Maurer (2020a) fragility functions, which are conditioned on *LPI*. As an example, the test and training set performance is shown in figure 3.2 for the ML model. Here, the "predicted probability" is the output when *LPI* was predicted via the geospatial ML model, whereas the "actual probability" is that when *LPI* was computed from the CPT data. Also shown in figure 3.2 are linear trendlines (green dotted lines), from which

assessments of overall prediction bias may be made. The ML model's MAEs of 3.58 and 3.72 (*LPI* units) on the training and test sets translate to MAEs of 7.17 percent and 7.65 percent in probability units (table 3.1). These comparisons (i.e., predicted vs actual probabilities of ground failure) provide the clearest context of model performance, given that the consequences of an *LPI* error vary widely depending on the *LPI* value. A prediction of *LPI* = 17, for example, is relatively erroneous if the actual *LPI* is 2, since this translates to a ~65 percent overprediction of ground-failure probability (Geyin and Maurer, 2020). In contrast, a prediction of *LPI* = 87 is very accurate if the actual *LPI* is 72, given that the probability of ground failure is nearly identical whether *LPI* is 87 or 72. For this reason, direct comparison between predicted and actual *LPI* values is less meaningful. As seen in figure 3.2, the model was generally unbiased on the training and test sets, but it did exhibit relatively more bias on the latter, such that the predicted probability of ground failure had an average tendency to be 2 percent greater than actual. This might be attributable to the dataset's modest size, such that the test set had features unrepresented in training.

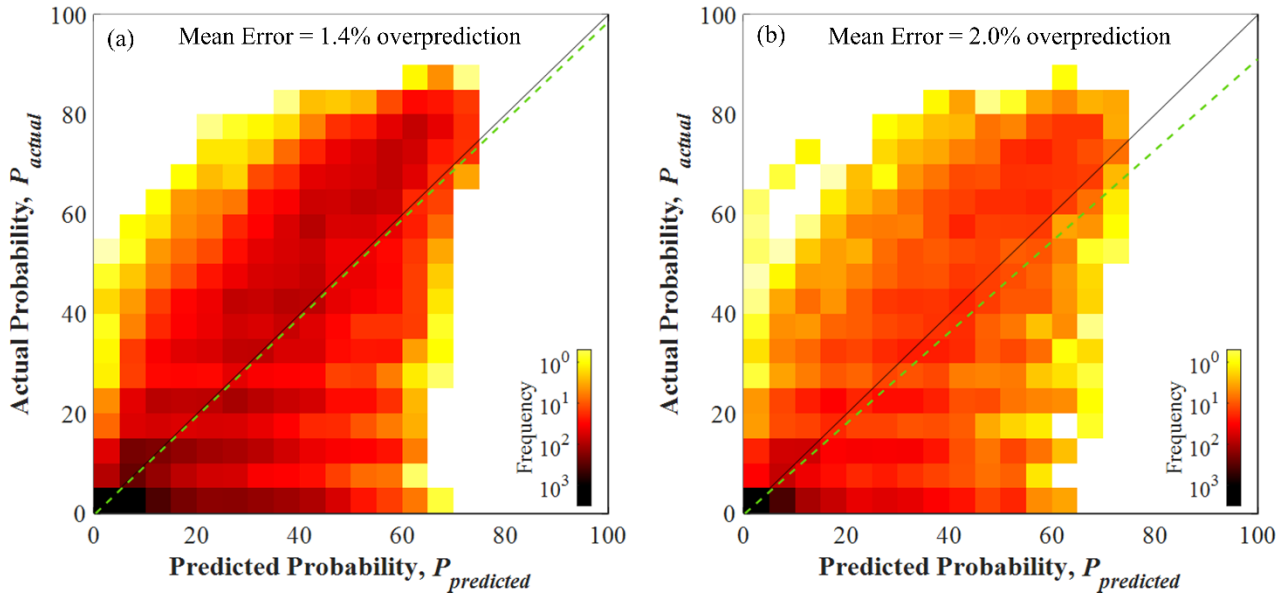

Figure 3.2 Probability of ground failure: ML prediction vs. actual for the (a) training dataset and (b) test dataset. Green dotted lines = linear trendlines, from which prediction bias may be judged

3.1. Field Application and Testing

To demonstrate and test forward predictions at regional scale, the ML, DL, and Ensemble models were next used to predict ground failure in eleven U.S. earthquakes across two types of

datasets. Performance was assessed by using field observations and was compared against the Rashidian and Baise (2020) model in all events. Because of the paucity of recent, well documented U.S. earthquakes outside of California, these tests covered a relatively narrow geographic range. Further testing on future events in other U.S. regions is thus needed.

In the first series of tests, regional scale predictions were compared to mapped observations of ground failure in six events: (i) 1989 M_w6.9 Loma Prieta, California; (ii) 1994 M_w6.7 Northridge, California; (iii) 2001 M_w6.8 Nisqually, Washington; (iv) 2003 M_w6.5 San Simeon, California; (v) 2011 M_w5.8 Mineral, Virginia and (vi) 2016 M_w7.1 Ridgecrest, California. In these events, mapped observations of liquefaction-induced ground failure were obtained from the USGS Ground Failure Database (Schmitt et al., 2017a,b), except for observations from the 2011 Mineral and 2016 Ridgecrest events, which were respectively obtained from Green et al. (2015) and Zimmaro et al. (2020). The quantities of mapped observations in these six events were, respectively, 129, 41, 44, 12, 35, and 2. In these datasets, mapped observations were exclusively "positive" (i.e., a lack of liquefaction was not explicitly mapped). It was therefore assumed that liquefaction did not manifest if none was documented, as had been previously assumed in the development of geospatial hazard models (e.g., Zhu et al., 2017). While this assumption may at times be invalid and inevitably introduces uncertainty, it facilitates rapid, regional-scale testing across a variety of topographic and geomorphic environments. In this regard, we viewed performance in the context of model comparisons and not as an absolute measure of efficacy. Later, a separate dataset containing positive *and* negative observations at discrete sites will be discussed.

For each earthquake, a USGS ShakeMap file with all requisite seismic data (i.e., M_w and mapped *PGA* and *PGV*) was obtained in .xml format. The adopted geospatial predictor variables were then compiled across the ShakeMap extents (i.e., the area of perceptible shaking). As an example, these inputs are mapped in figure 3.3 for the 1989 Loma Prieta earthquake. It can be seen in the final two panels of figure 3.3 that while unconsolidated soil covered ~40 percent of the study area, the dominant soil type was infrequently mapped as either sand, silt, or clay. Although soil lithology was always defined in the Horton et al. (2017) compilation, it was not always used by the models developed herein for one of two reasons. First, not all dominant soil types were found to be useful in the early stages of modelling. Some mapped soil types (e.g., marl, gravel, peat) had insufficient in-situ test data to elucidate and quantify the relationship between soil type and liquefaction hazard. Second, the mapped lithology was sometimes not predicted to a useful degree

of specificity (e.g., as “sand” or “clay”), but rather was defined only as “coarse detrital” or “fine detrital.” These broad classifications were similarly found not to be useful, which might be expected given that particle gradation is generally not efficient or sufficient for classifying liquefaction hazard. Accordingly, the model benefitted from knowledge of the mapped soil type when it was clay, sand, or silt, whereas if the mapped soil type was not one of these classifications, it was inherently treated as having a general unconsolidated character. It is likely that additional geologic descriptors would be useful to future models that use larger and more diverse sets of training data. Following compilation of the adopted geospatial predictor variables, probabilities of ground failure were computed using the three models developed herein and RB20. These probabilities are mapped in figure 3.4 for the 1989 Loma Prieta earthquake, along with observations of ground failure.

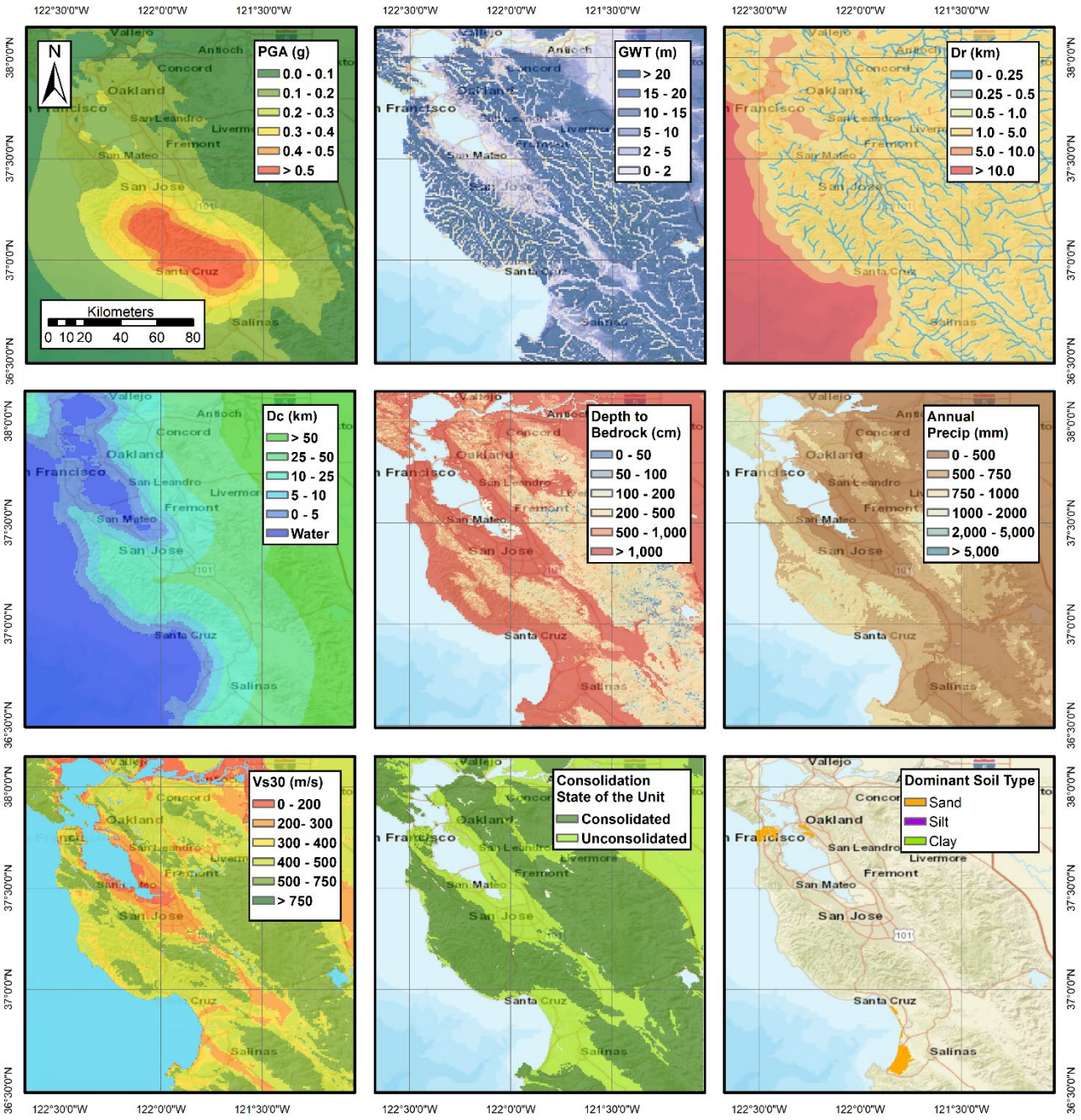

Figure 3.3 Model predictor variables mapped across the area affected by the 1989 Loma Prieta earthquake

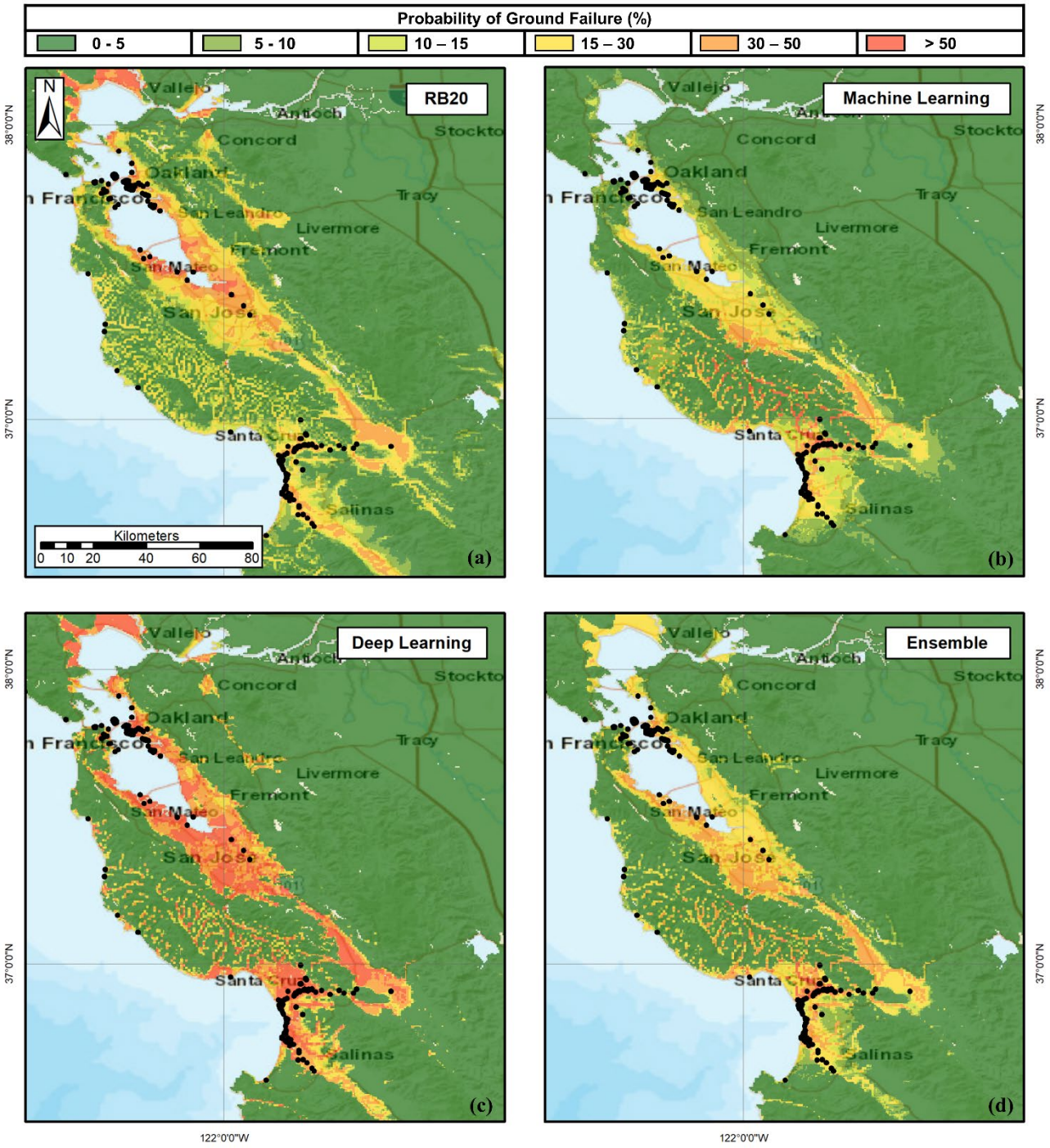

Figure 3.4 Probabilities of ground failure for the 1989 Loma Prieta earthquake, as computed by the (a) RB20; (b) ML; (c) DL; and (d) Ensemble models. Black dots are observed ground failures.

Model performance was quantified by using ROC *AUC* values, as is common for binomial classifiers, and which give equal weighting to false positive and false negative predictions. Samples were collected on a 100-m by 100-m grid across the ShakeMap extents. Grids wherein ground

failures were observed were classified as “positive” and those without any documented evidence as “negative.” This resulted in several million data points per event, although the exact quantity depended on the event’s area of influence. While the method of geospatial sampling has been shown to influence computed *AUC* values (Lin et al., 2021a) (e.g., if an equal number of positive and negative points were sampled instead), we found that *relative* performance was insensitive to this decision (i.e., the best and worst models were the same in each event across a range of sampling techniques). Plotted in figure 3.5 are ROC curves for each model in the 1989 Loma Prieta earthquake from which *AUC* values were computed. Arranged by *AUC*, the best performing models were RB20 (*AUC* = 0.949), Ensemble (*AUC* = 0.945), DL (*AUC* = 0.944), and ML (*AUC* = 0.931). The four models thus exhibited very similar efficiencies, with the Ensemble model slightly outperforming the individual ML and DL models. Following the same methodology, analyses were performed for the 1994 Northridge and 2001 Nisqually events, as mapped in figure 3.6, and for the 2011 Mineral and 2016 Northridge events, as mapped in figure 3.7. A summary of model performance—was quantified by *AUC*—is presented in table 3.2 for these events and others yet to be discussed. It can be seen that RB20 outperformed the Ensemble model for three of the six events. Specifically, for Loma Prieta by 0.4 percent, for Northridge by 3.5 percent, and for Nisqually by 1.3 percent. Conversely, the Ensemble model outperformed RB20 for San Simeon by 0.3 percent, for Mineral by 2.9 percent, and for Ridgecrest by 1.4 percent. The models proposed herein thus demonstrated efficacies similar to those of RB20 for these specific events. While these measured differences in performance fluctuate with different sampling techniques, the overall conclusion of apparently similar performance remains the same. In subsequent analyses, it will be determined whether these measured differences in performance were statistically significant.

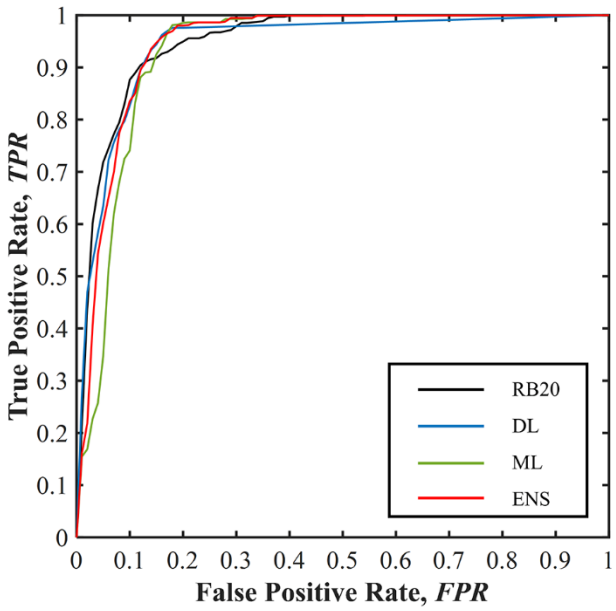

Figure 3.5 Receiver operating characteristic (ROC) curves for the RB20, DL, ML, and Ensemble models

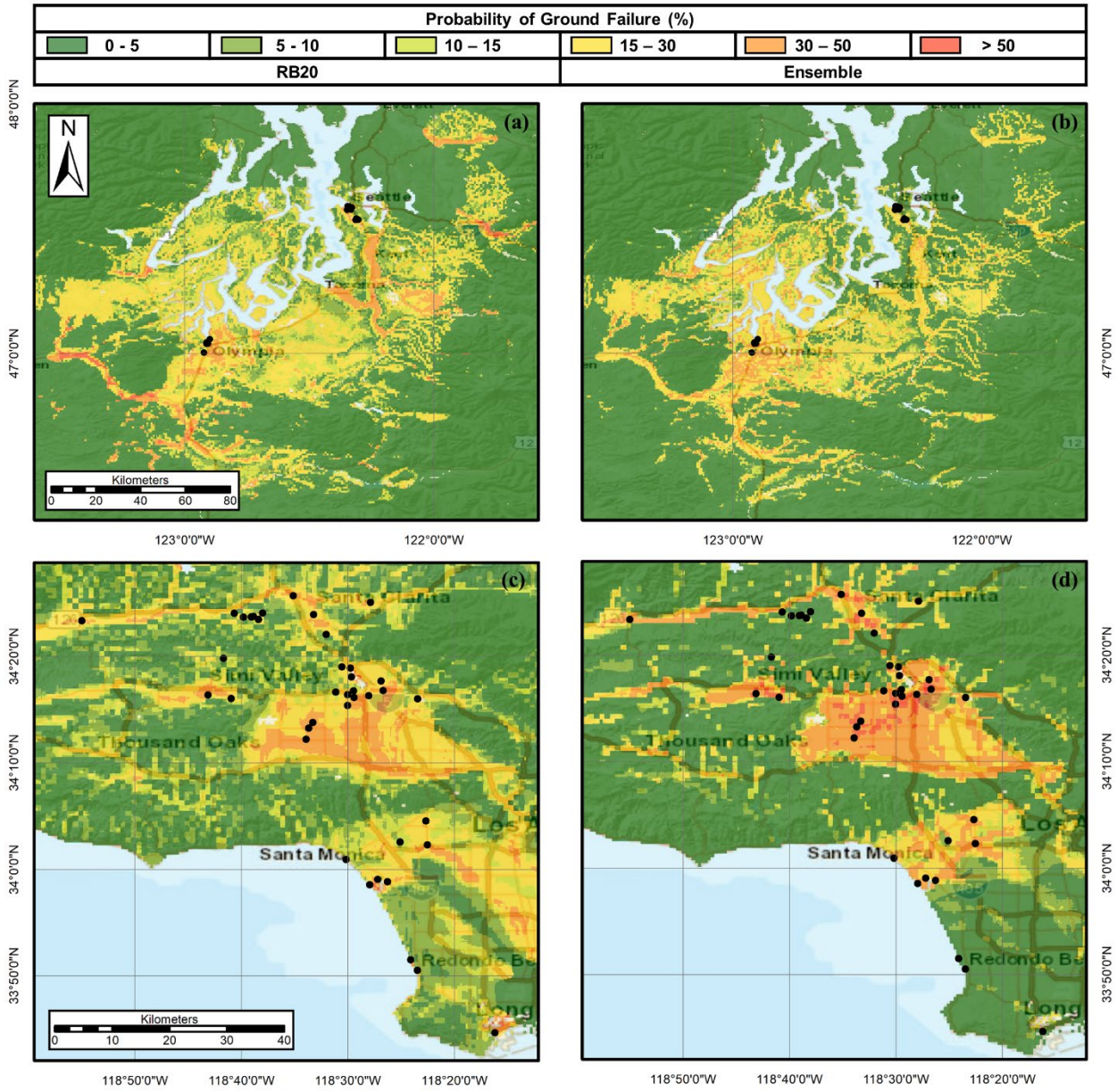

Figure 3.6 Probabilities of ground failure for the 2001 Nisqually earthquake, as computed by (a) RB20 and (b) the Ensemble model; and for the 1994 Northridge earthquake, as computed by (c) RB20 and (d) the Ensemble model. Black dots are observed ground failures.

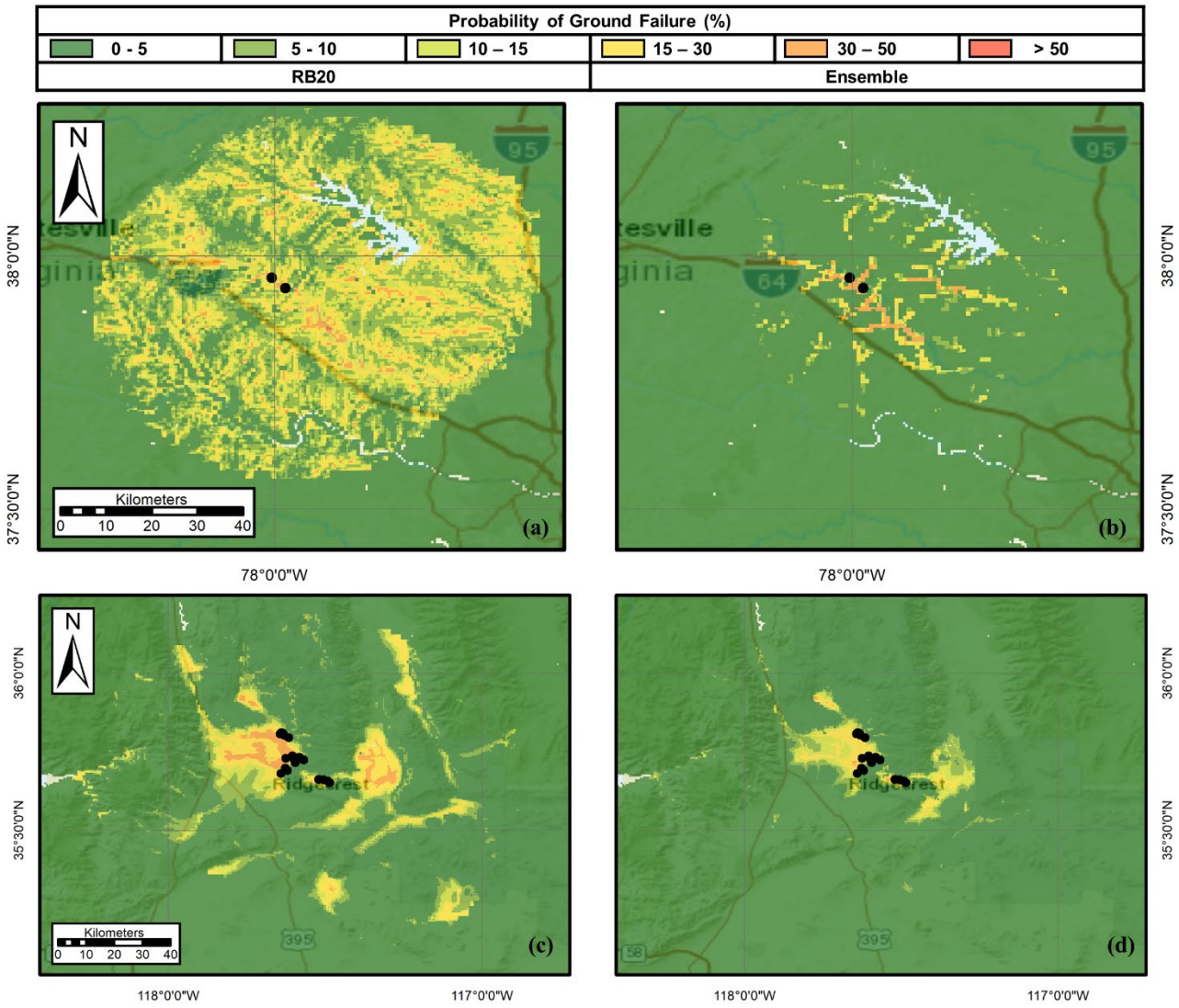

Figure 3.7 Probabilities of ground failure for the 2011 Mineral earthquake, as computed by (a) RB20 and (b) the Ensemble model; and for the 2016 Ridgecrest earthquake, as computed by (c) RB20 and (d) the Ensemble model. Black dots are observed ground failures.

Table 3.2 Summary of AUC values for events and datasets described in the text, as computed for the ML, DL, and Ensemble models developed herein, and for the RB20 model.

Model	Dataset 1						Dataset 2
	Loma Prieta	Northridge	Nisqually	San Simeon	Mineral	Ridgecrest	101 Case Histories
DL	0.944	0.803	0.931	0.665	0.655	0.992	0.682
ML	0.931	0.812	0.920	0.980	0.733	0.945	0.765
Ensemble	0.945	0.813	0.933	0.979	0.732	0.992	0.734
RB20	0.949	0.848	0.946	0.976	0.703	0.978	0.504

Additional observations from figures 3.4 through 3.7 and table 3.2 are as follows. *First*, with respect to model bias, the RB20 model was either originally trained (by Zhu et al., 2017) or later calibrated (by Rashidian and Baise, 2020) using the same observational data adopted herein for testing, except for the Ridgecrest earthquake data, which postdated Rashidian and Baise (2020). In contrast, the ML/DL models were trained on CPTs from areas affected by the Loma Prieta, Northridge, and San Simeon events, but not directly on the field observations adopted for testing. Moreover, the Nisqually, Mineral, and Ridgecrest earthquakes provided completely blind tests of the ML/DL models, since no data from these events/regions were included in training. While a more rigorous analysis of bias was not undertaken, nor critical to the thesis of this study, we nonetheless note that the preceding tests were generally biased in favor of RB20.

Second, it was observed that the DL model was relatively sensitive to predicted water table depth, in comparison to the ML and RB20 models. In this regard, erroneous predictions by the DL and Ensemble models were often associated with erroneous expectations of the groundwater depth. As an example, predictions for the 2003 San Simeon earthquake by the DL and RB20 models are mapped in figure 3.8. Specifically, an area near the towns of Oceano and Grover Beach, California, is shown, where numerous ground failures were observed, as mapped in figure 3.8. Because the Fan and Miguez-Macho (2020) model predicted a groundwater depth of ~20 m beneath the northernmost features, the DL model predicted a near-zero probability of ground failure, whereas RB20 generally predicted a probability of 5 to 15 percent. Due largely to this behavior, the DL and RB20 models had respective *AUC*s of 0.665 and 0.976 for this event. To assess the influence of more accurate inputs, nearby well measurements were obtained from the California Department of Water Resources (DWR, 2020), indicating that groundwater was shallower in this area than expected by Fan and Miguez-Macho (2020). Using this more accurate input, the models were rerun, as mapped in figure 3.8. While the RB20 and ML models correspondingly displayed slight improvements (~1 percent increase in *AUC*), the DL model's *AUC* increased nearly 30 percent to 0.990. Similar behavior could be observed in other events at a lesser scale, from which we concluded that the performance of the DL model would likely improve with more accurate groundwater maps.

Third, considering the three models developed herein, the Ensemble model outperformed both the ML and DL models in three events. The ML model performed best in two other events, and in the last event the DL and Ensemble models tied for best performance. Considering all tests

(i.e., both the blind prediction of *LPI* and the regional-scale prediction of ground failure), the DL model lacked statistical support for individual use. Accordingly, and in conjunction with the DL model's sensitivity to groundwater data, we recommend adoption of the ML or Ensemble models. Ultimately, additional tests in other events, and ideally additional model training and improvements, are needed before one model is recommended over another.

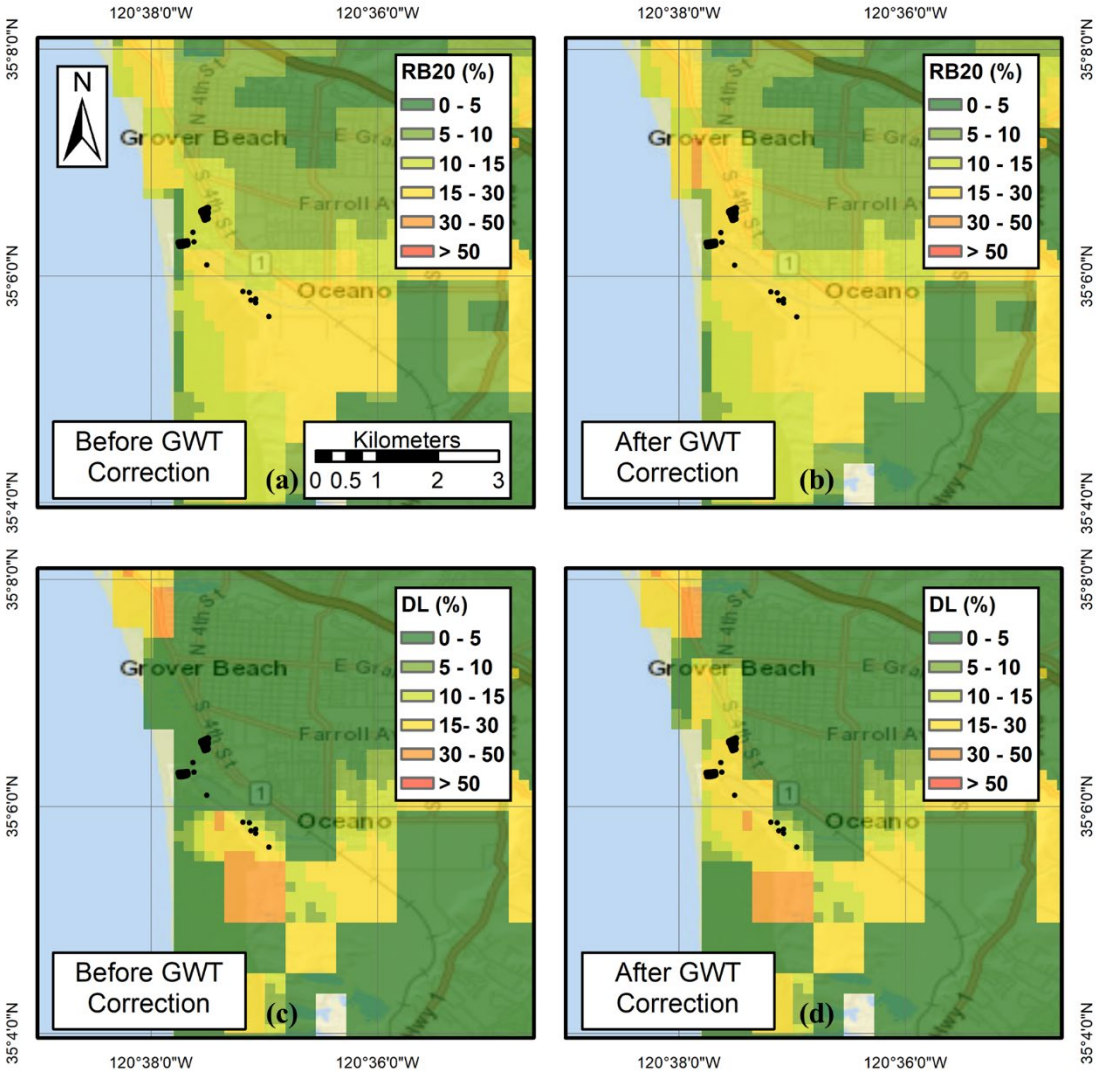

Figure 3.8 Probabilities of ground failure in the 2003 San Simeon earthquake, with and without correction of measured ground water table (GWT) depths: (a) RB20 before GWT correction; (b) RB20 after GWT correction; (c) DL model before GWT correction; and (d) DL model after GWT correction. Black dots are observed ground failures.

Toward that end, a second dataset of 101 well-documented liquefaction case histories was also used to test performance. These cases, which consisted of both positive *and* negative

observations, were sourced from Geyin and Maurer (2021a), who compiled from the literature all CPT-based case histories from all earthquakes in the U.S. to date. Namely, the (i) 1971 M_w7.6 San Fernando; (ii) 1979 M_w7.6 Imperial Valley; (iii) 1981 M_w5.9 Westmoreland; (iv) 1983 M_w6.9 Borah Peak; (v) 1987 M_w6.2 Elmore Ranch; (vi) 1987 M_w6.5 Superstition Hills; (vii) 1989 M_w7.6 Imperial Valley; and (viii) 1994 M_w6.9 Northridge earthquakes. In the resulting compilation, liquefaction manifestations were observed in 57 percent of cases and were not observed in the remaining 43 percent. The four geospatial models were applied to each event, and *AUC* values were computed for the composite dataset, as given in table 3.2. In this analysis, the ML/DL models performed much better than RB20, which had an *AUC* near 0.5, an efficiency akin to random guessing. Of the models developed in this study, the ML model performed best (*AUC* = 0.765). In contrast to the initial series of tests, however, those using this second dataset might have been biased in favor of the ML/DL models, since some of the 101 sites held CPTs included in the dataset of the 1,712 used in model development. While these tests provided another datapoint for consideration, wherein it is known with confidence that the field observations were correctly classified, we prefer not to glean definitive new conclusions, given the possibility of bias and the small size of the dataset.

Lastly, to assess whether the findings presented thus far might change with consideration of finite-sample uncertainty, P-values were computed using the nonparametric method of DeLong et al. (1988) to assess whether differences in *AUC* could result by chance (i.e., due to limited field data) and not because one model was more efficient than another. The P-values computed by this approach were probabilities that two *AUC* samples could have come from the same distribution. Since this approach required *AUC* normality, Anderson-Darling and Lilliefors tests (Anderson and Darling 1952; Lilliefors 1967) were used to confirm that all samples came from a normal distribution. P-values were computed to compare each model to all others in the six regional analyses and in the dataset of CPT case histories. These values, which indicated whether differences in model performance were statistically significant, are presented in table 3.3. A significance level of 0.05 was adopted, such that P-values below 0.05 were deemed significant. All else being equal, small P-values could be expected when: (i) differences between two *AUC* values were large; or (ii) the uncertainties of *AUC* values were small; or (iii) distributions have high correlation. Using this criterion, table 3.3 compares all model pairs and identifies which was significantly better. The model with the better *AUC*, as reported in table 3.2, is indicated in table 3.3 via the cell shading. If the cell is shaded orange, the model in the left column was better, whereas if the model in the top

row was better, the cell is shaded grey. The values given in each cell are the P-values; those less than 0.05 are highlighted via bold font and a red border. Table 3.3 can thus be used to determine whether differences in model performance, as first presented in table 3.2, were statistically significant. Notable observations from table 3.3 are as follows:

(i) In the initial series of six events at regional scale, the Ensemble model was significantly better than RB20 in two events (Mineral and Ridgecrest), RB20 was significantly better than the Ensemble model in one event (Northridge), and the two models were statistically indifferent in the remaining three (Loma Prieta, Nisqually, and San Simeon).

(ii) In the analysis of CPT case history sites, the Ensemble, ML, and DL models were significantly better than RB20.

Collectively, these results suggest that the ML/DL models, which were trained on a modest dataset, predicted ground failure with efficiency that was similar to or better than that of RB20 and thus warrant further application, evaluation, and development. And, as is common in the prediction of ground motions, storm tracks, and other natural hazards, the proposed prediction models could be ensembled with other geospatial liquefaction models, thereby capturing the epistemic uncertainty of model development.

Table 3.3 P-value matrix to compare model performance. ML = machine learning model; DL = deep learning model; RB20 = Rashidian and Baise (2020); and ENS = ensemble of ML and DL models, as described in the text

Statistically Better	↑	Nisqually			Loma Prieta			San Simeon			Northridge			Ridgecrest			Mineral			CPT Case Histories		
←		DL	RB20	ENS	DL	RB20	ENS	DL	RB20	ENS	DL	RB20	ENS	DL	RB20	ENS	DL	RB20	ENS	DL	RB20	ENS
Nisqually	ML	0.484	0.285	0.405																		
	DL		0.221	0.473																		
	RB20			0.334																		
Loma Prieta	ML				**0.004**	**0.002**	**0.000**															
	DL					0.138	0.596															
	RB20						0.278															
San Simeon	ML							**0.000**	0.370	0.341												
	DL								**0.000**	**0.000**												
	RB20									0.321												
Northridge	ML										0.440	0.055	0.613									
	DL											**0.003**	0.279									
	RB20												**0.036**									
Ridgecrest	ML													**0.001**	**0.017**	**0.002**						
	DL														**0.015**	0.341						
	RB20															**0.016**						
Mineral	ML																0.124	**0.001**	0.666			
	DL																	0.396	0.121			
	RB20																		**0.002**			
CPT Case Histories	ML																			**0.009**	**0.000**	0.057
	DL																				**0.000**	**0.004**
	RB20																					**0.000**

*Cell values are the P-values (i.e., probabilities) that *AUC* samples from two prediction models could have come from the same parent distribution (i.e., be statistically indifferent). The model with better *AUC*, as reported in Table 4, is indicated via the cell shading. Values less than 0.05 are deemed "significant" and are highlighted via bold font and a red border.

3.2. Software Implementation

Arguably, a limitation of any ML/DL model is the lack of a defined analytical expression easily ported and executed via hard copy. By corollary, simple interpretations of model structure and form are also generally lacking. While these detractions may be significant to traditionalists, it is clear the use of algorithmic learning will only grow in the field of geotechnics and geohazards, given its demonstrated capabilities when provided with large datasets. It is critical, however, that trained ML/DL models be provided as code, ideally in a format accessible to a broad userbase. Despite this necessity, enumerable ML/DL models have been published without code, meaning that while a model may be available for use by the respective developers, it is not easily accessed by the broader community and is therefore not readily applied, tested, or improved upon by others.

To facilitate user adoption and evaluation, the ML, DL, Ensemble, and RB20 models were programmed into *RapidLiq* (Geyin and Maurer, 2021b), a new Windows software program with a simple-to-use interface (figure 3.9). While the Rashidian and Baise (2020) model is widely referenced, it is not commonly implemented by individual users because of the predictor variables that must first be compiled. These variables, and those of the proposed models, are compiled within *RapidLiq*, making user implementation trivial. The only required input is a ShakeMap of ground-motion parameters (i.e., *PGA*, *PGV*, M_w), either in Extensible Markup Language (.xml) or Geotagged Image File (.tiff) format. The first is easily downloaded from the USGS earthquake catalog (https://earthquake.usgs.gov/earthquakes/search/) minutes after an earthquake, or for numerous future scenario events. The second is a more general, flexible format, allowing for motions from various sources to be analyzed. The software then extracts predictor variables across the ShakeMap extents and outputs geotiff files mapping the probabilities of liquefaction-induced ground failure. These files may be viewed within the software or explored in greater detail using GIS or one of many free geotiff web explorers (e.g., http://app.geotiff.io/). The software also allows for tabular input, should a user wish to enter specific sites of interest and ground-motion parameters at those sites, rather than study the regional effects of an earthquake. At present, *RapidLiq* operates in the contiguous U.S. and completes predictions within 10 s for most events.

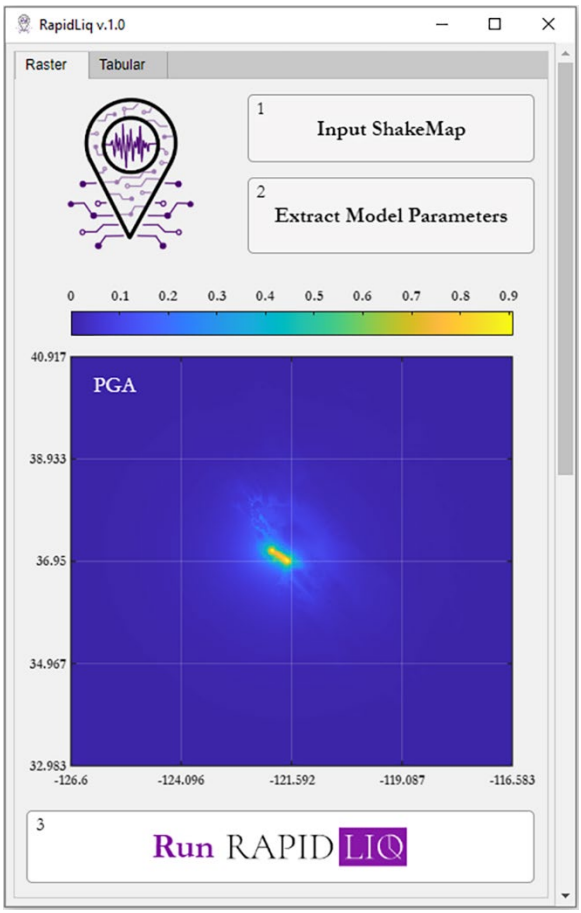

Figure 3.9 User interface of *RapidLiq* (Geyin and Maurer, 2021b), which runs the ML, DL, Ensemble, and RB20 models. *RapidLiq* may be downloaded from: https://doi.org/10.17603/ds2-4bka-y039

3.3. Modeling Limitations and Uncertainties

The geospatial models developed and tested herein are best suited for regional-scale applications where subsurface testing is infeasible (e.g., disaster simulation and loss estimation; planning and policy development; and emergency response and reconnaissance) or for preliminary site assessment in advance of subsurface testing. While such models have recently been adopted for a variety of uses, they are not intended to guide engineering design and do not replace the need for rigorous site-specific analyses of liquefaction hazard. In this regard, the proposed models predict liquefaction at a relatively coarse spatial resolution, given the resolutions of the geospatial predictor variables (see table 3.2), and can thus easily fail to capture more localized, small-scale features that correlate to higher or lower liquefaction hazard.

Inherently, the findings presented herein are tied to the data analyzed. The applicability of these findings to other earthquakes elsewhere – particularly in regions underrepresented in model training – is unknown. Similarly, using the models beyond the range of the predictor variables studied herein (table 3.2) could likewise introduce greater uncertainty. In addition, it should be emphasized that "ground failure," the ultimate prediction target, refers to free field liquefaction-induced surface settlement, cracking, and ejecta on ground that is generally level. Users should understand the limitations of the *LPI* manifestation model to predict lateral spreading, which is a distinctly damaging expression influenced by complex subsurface and topographic features. Given that *LPI* and other similar manifestation models may be poor predictors of lateral spreading (e.g., Maurer et al., 2015b; Rashidian and Gillins, 2018), the proposed models may likewise predict it poorly. In this regard, the ground-failure datasets on which the models were tested might include lateral spreads, which could have the effect of reducing the measured model efficiency. Moreover, the proposed models do not explicitly predict damage to specific infrastructure types or assets, which would require detailed site and asset-specific modeling. In this respect, liquefaction could trigger at depth and damage infrastructure without otherwise manifesting or could manifest without otherwise causing damage.

As discussed herein, the performance of any geospatial model is inherently tied to the resolution and accuracy of predictor variables, some of which are themselves predictions rather than measurements (e.g., the depth of groundwater). Inherently, the accuracy of liquefaction predictions is related to the accuracy of inputs, with some models having greater sensitivity to specific inputs. In the present effort, measurement and modeling uncertainties were not considered, and as such, the model outputs should be considered to be median probabilities of ground failure. This should not be interpreted to mean that uncertainties do not exist. Among other uncertainties that could be considered in the future, ShakeMap IMs are uncertain; the prediction of *LPI* via geospatial variables is uncertain; and *LPI* is an uncertain predictor of ground failure. In the future, ML/DL techniques (e.g., Gaussian Process Regression) could be used to account for these uncertainties and make probabilistic predictions. Additionally, the most efficient geotechnical models for predicting liquefaction will inevitably change over time. In this regard, the proposed approach could be conditioned on models other than *LPI*, to include emergent mechanistic methods that may better capture the system-level response of soil profiles

(e.g., Cubrinovski et al., 2019; Bassal and Boulanger, 2021; Hutabarat and Bray, 2021). For the present moment, the models proposed herein appear to perform as well as, and potentially better than, the current state-of-practice geospatial model (i.e., RB20), but they were developed using an altogether different approach, and thus warrant further application. Ultimately, additional tests in past or future events are needed to confirm the findings presented herein and summarized in Chapter 5.

CHAPTER 4. APPLICATION TO BRIDGE SITES IN WASHINGTON STATE

To demonstrate application of the developed models to transportation infrastructure (whether in advance of an earthquake for planning and mitigation, or immediately after an event for response and recovery), the models were used to predict liquefaction-induced ground failure at bridge sites in Washington state affected by a magnitude 9, Cascadia Subduction Zone earthquake.

4.1. Simulated Cascadia Subduction Zone Ground Motions

Researchers at the United States Geological Survey (USGS) and the University of Washington (UW) collaborated to produce 30 sets of synthetic seismograms of magnitude 9 Cascadia Subduction Zone earthquakes. These ground motion simulations were produced by combining synthetic seismograms derived from 3D finite-difference simulations with finite-source, stochastic synthetics (Frankel et al. 2018). The 30 synthetic seismograms included a range of rupture parameters to capture a wide range of possible M9 events (Frankel et al. 2018). Varied rupture parameters included the hypocenter of the motion, the rupture velocity, and the magnitude and location of subevents (Wirth et al. 2018). Using Pacific Northwest shear-wave velocity profiles, soil-adjusted ground motions were produced using equivalent linear site response analysis (de Zamacona 2019). Predicted maximum shear strains within the profiles were generally below proposed limits for judging the credibility of equivalent linear site-response analyses (e.g., Kaklamanos et al. 2013). Nonetheless, the possibility persists, for select motions at select sites, that the equivalent-linear treatment of nonlinear soil behavior could result in differences between the motions predicted by de Zamacona (2019) and studied herein, and those that might be produced using other treatments of nonlinear behavior. Many additional details pertaining to the simulated motions may be found in Frankel et al. (2018), Wirth et al. (2018), de Zamacona (2019), and Kortum et al. (2021).

4.2. Predictions of Ground Failure at Bridge Sites

Using the RB20, ML, DL, and Ensemble models, probabilities of liquefaction-induced ground failure were predicted at the locations of 5,020 bridges in Washington state, as compiled from the National Bridge Inventory. These predictions were made for each of the 30 M9 ground-motion simulations. As an example, predictions made by the Ensemble model are mapped across Washington state in figure 4.1 for one of the 30 ground-motion simulations.

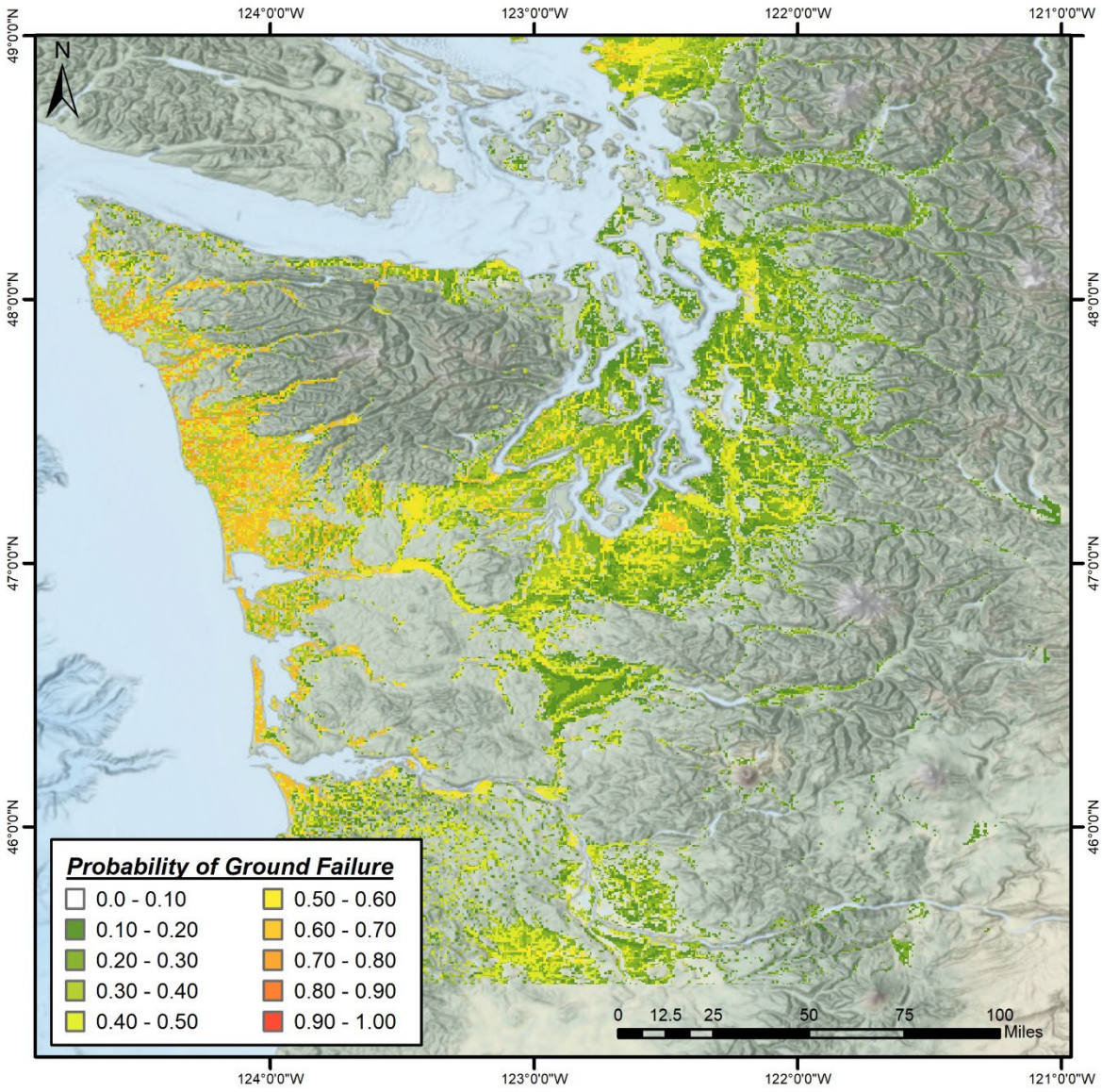

Figure 4.1 Probability of ground failure in one of 30 M9 earthquake simulations, as computed using the proposed ML/DL Ensemble model

To arrive at an initial, surficial understanding of liquefaction hazard at bridge sites, predictions from all 30 ground-motion simulations were coalesced in the form of a median prediction at every location. Mapped in figure 4.2, for each of the 5,020 bridges, is the median probability of ground failure in an M9 CSZ event, as computed by the Ensemble model.

The most salient results of these analyses included the following: (i) the median probability of ground failure ranged from 0 percent (800 bridges) to 72 percent (three bridges); (ii) 13 bridges had at least a 70 percent probability of ground failure; (iii) 218 bridges had at least

a 60 percent probability of ground failure; and (iv) 795 bridges had at least a 50 percent probability of ground failure. In general, bridges on sites with the greatest probability of ground failure were located either on the Washington Coast (particularly near rivers, estuaries, and bays surrounded by flat ground) or in similar settings within the Puget Sound. Shown in figure 4.3 are select bridges along the I-5, I-405, and I-90 corridors in the vicinity of Seattle. Considering this subset, bridges with the largest probability of ground failure (50 percent to 60 percent) were in the Snohomish River Delta near Everett, as indicated in figure 4.3 via a red box. This area is shown in greater detail in figure 4.4. Additionally, observed liquefaction features in this area, as discovered and compiled by Bourgeois and Johnson (2001), are also mapped in figure 4.4. While the prevalence of these features, which predate modern settlement (ca. 1850), is unknown, their extent and severity speak to the high liquefaction hazard of the area. As an example, one such feature is shown in figure 4.5, as photographed during a site investigation by the authors. Similar liquefaction features were observed around the abutments of I-5 and SR 529 bridges, which may be seen on the horizon in figure 4.5. While discrepancies between observed and predicted liquefaction would not necessarily discredit the latter, their agreement nonetheless lent credence to the developed models and results.

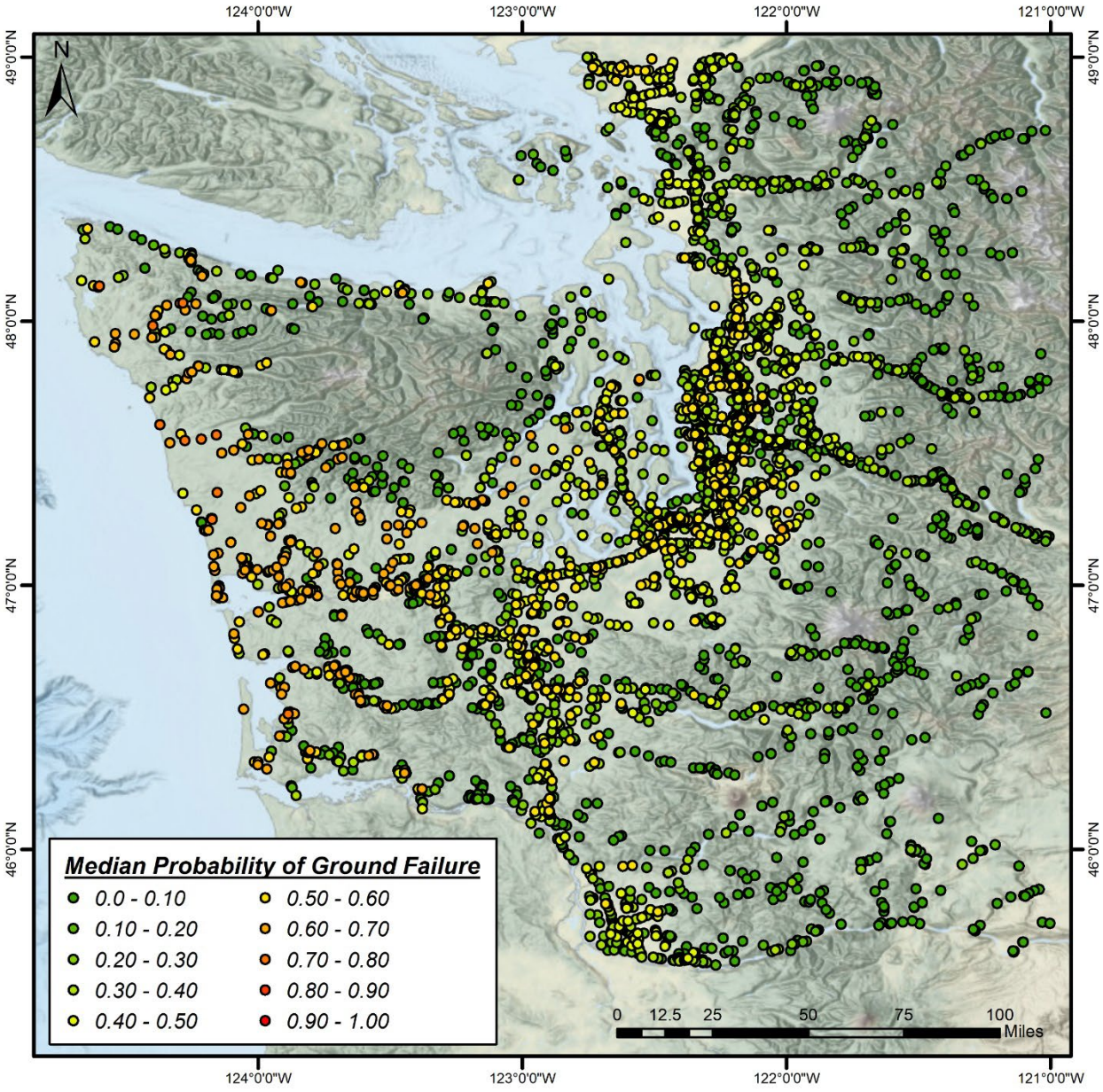

Figure 4.2 Median probability of ground failure at 5,020 bridge sites in Washington state, as computed using the proposed ML/DL Ensemble model

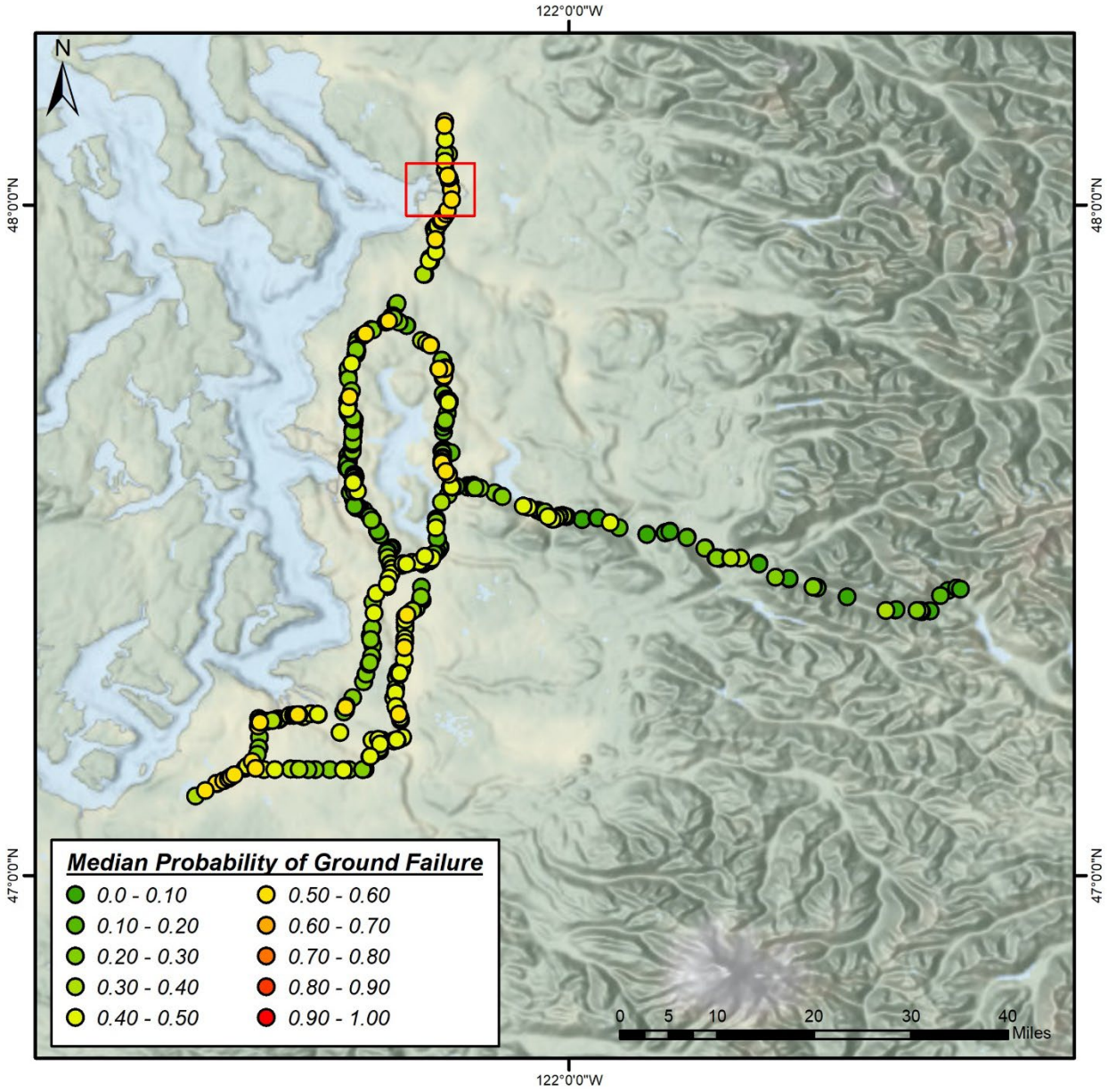

Figure 4.3 Median probability of ground failure at select bridge sites along the I-5/I-90 corridors in Washington state, as computed using the proposed ML/DL Ensemble model. Among the bridges considered, those with the greatest probability of ground failure were found in the Snohomish River delta, denoted by a red box and shown in greater detail in figure 4.4

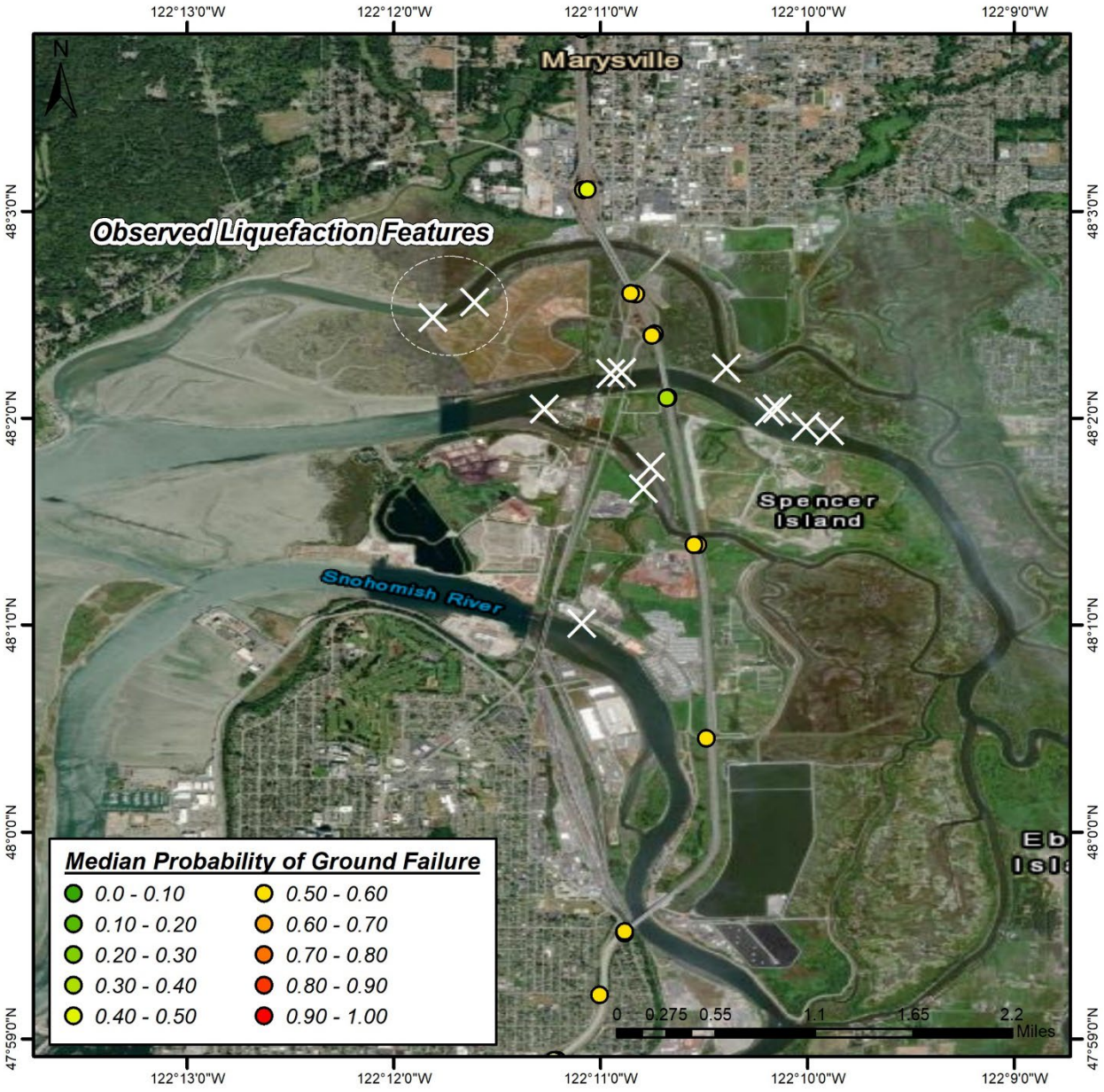

Figure 4.4 Median probability of ground failure at bridge sites near the Snohomish River delta, as computed using the proposed ML/DL Ensemble model. Also shown are observed liquefaction features in the area, as compiled by Bourgeois and Johnson (2001)

Figure 4.5 A 1-m diameter liquefaction vent along the Snohomish River. Visible on the horizon is an I-5 bridge. Other similar features surround the I-5 bridge abutments, as well as those of other area bridges.

Notably, these analyses did not consider specific bridge designs or site-specific ground improvement works that may or may not have been carried out. The analyses did, however, provide a ranked list of bridge sites most likely to be damaged by ground failure. Select ground truthing lent credence to the developed models and predictions. These predictions may be further investigated (e.g., via network analyses) to identify critical corridors likely to experience outages and/or to prioritize bridges for more advanced studies and possible earthquake retrofitting. While the results serve an important purpose and may be made rapidly for any past or future earthquake, they are inherently first-order in nature. In-situ test data and subsequent liquefaction modelling would be needed to confirm predictions at any bridge site

.

CHAPTER 5. CONCLUSIONS

This study proposed a new approach to geospatial modelling of soil liquefaction that is driven by algorithmic learning but pinned to a mechanistic framework. In effect, subsurface measurements are predicted remotely within the framing of a popular model for probabilistically predicting ground failure. This merges a body of knowledge built over the last 50 years with the potential of machine and deep learning to predict subsurface conditions remotely. As hypothesized herein, this modelling approach has potential advantages over others used to date. Using this approach, three models termed ML, DL, and Ensemble were trained on a dataset of CPTs distributed across the U.S. using a modest set of ten geospatial predictor variables. These models were shown to provide efficient predictions in unbiased, forward application and were tested against the RB20 geospatial model. Collectively, these tests indicated that the proposed models predict ground failure with an efficiency similar to or better than that of RB20 and thus warrant application and further evaluation. The proposed and RB20 models are available in *RapidLiq*, a free Windows program that may be downloaded from https://doi.org/10.17603/ds2-4bka-y039.

Ultimately, significantly more in-situ geotechnical tests are available for model training, both in the U.S. and specifically in Washington state. The performance of the model in Washington State was particularly notable (e.g., for the 2001 Nisqually earthquake), given the lack of training data sourced from the region. Whereas ground-failure inventories are likely to grow slowly, with data from perhaps several events per year impacting a small fraction of Earth, the subsurface data needed to train the proposed approach exist in massive quantities. These data require compilation across different formats (some requiring digitization) and test types (e.g., CPTs and SPTs), as well as access from various entities, both public and private. However, community geotechnical datasets in New Zealand, Austria, Germany, and Italy, for example, currently contain more than 40,000 CPTs. Similar datasets are likely to be created elsewhere. Approximately 1,000 CPTs may be publicly available in Washington state, along with many thousands or tens of thousands of SPTs, but these tests all generally require digitization. Likewise, the quantity of prospective geospatial predictor variables exceeds that utilized in this study. Expanding upon the general approach proposed herein, improved geospatial liquefaction models could thus be developed for state, regional, or national application in a subsequent study.

In this regard, Washington state shows particular promise for a state-specific model, given the potential availability of large quantities of training data.

CHAPTER 6. REFERENCES

Anderson, T.W. and Darling, D.A. 1952. Asymptotic theory of certain" goodness of fit" criteria based on stochastic processes. *The annals of mathematical statistics,* 23(2): 193-212.

Auret, L. and Aldrich, C. (2011). Empirical comparison of tree ensemble variable importance measures. *Chemometrics and Intelligent Laboratory Systems,* 105(2): 157-170.

Bassal, P.C., and Boulanger, R.W. (2021). System response of an interlayered deposit with spatially preferential liquefaction manifestations. *Journal of Geotechnical and Geoenvironmental Engineering*, 147(12): 05021013.

Boulanger, R.W. and Idriss, I.M. (2014). *CPT and SPT Based Liquefaction Triggering Procedures, Report No. UCD/CGM-14/01*, Center for Geotechnical Modeling, University of California, Davis, CA.

Bourgeois, J. and Johnson, S.Y. 2001. Geologic evidence of earthquakes at the Snohomish delta, Washington, in the past 1200 yr. *Geological Society of America Bulletin,* 113(4), 482-494.

Box, G.E.P and Cox, D.R. 1964. An analysis of transformations. *Journal of the Royal Statistical Society, Series B*. 26 (2): 211–252.

Brieman, L. 1996. Bagging predictors. *Machine Learning,* 24 (2): 123–140.

Cubrinovski, M. and Ishihara, K. 1998. State concept and modified elastoplasticity for sand modeling, *Soils and Foundations,* 38(4): 213-225.

Cubrinovski, M., Rhodes, A., Ntritsos, N., and Van Ballegooy, S. 2019. System response of liquefiable deposits. *Soil Dynamics and Earthquake Engineering*, 124: 212-229.

De Zamacona Cervantes, G. 2019. Response of Idealized Structural Systems to Simulated M9 Cascadia Subduction Zone Earthquakes Considering Local Soil Conditions. Master's Thesis, University of Washington, Seattle.

DeLong, E.R., DeLong, D.M., and Clarke-Pearson, D.L. 1988. Comparing the areas under two or more correlated receiver operating characteristic curves: a nonparametric approach. *Biometrics,* 44: 837-845.

Durante, M.G. and Rathje, E.M. 2021. An exploration of the use of machine learning to predict lateral spreading. *Earthquake Spectra*, 37(4): 2288–2314.

DWR (2020) Periodic groundwater measurements. *California Department of Water Resources*, <https://sgma.water.ca.gov/webgis/?appid=SGMADataViewer#gwlevels> last accessed June 2020.

Elith, J., Leathwick, J.R., and Hastie, T. 2008. A working guide to boosted regression trees. *Journal of animal ecology, 77*(4): 802-813.

Fan, Y., Li, H., and Miguez-Macho, G. 2013. Global patterns of groundwater table depth. *Science,* 339 (6122): 940-943, doi:10.1126/science.1229881

Fan, Y., Li, H., and Miguez-Macho, G. 2020. Updated dataset for global patterns of groundwater table depth. <http://thredds-gfnl.usc.es/thredds/catalog/GLOBALWTDFTP/catalog.html> last accessed July 2021.

Fawcett, T. 2006. An introduction to ROC analysis. *Pattern Recognition Letters,* 27(8): 861–874.

Federal Emergency Management Agency (FEMA) (2013). *Earthquake Model HAZUS-MH 2.1 Technical Manual*, Washington, D.C.

Fick, S.E. and Hijmans, R.J. 2017. WorldClim 2: new 1-km spatial resolution climate surfaces for global land areas. *International Journal of Climatology,* 37(12): 4302-4315.

Frankel, A.D., Wirth, E.A., Marafi, N., Vidale, J.F., and Stephenson, W.J. 2018. Broadband Synthetic Seismograms for Magnitude 9 Earthquakes on the Cascadia Megathrust Based on 3D Simulations and Stochastic Synthetics, Part 1: Methodology and Overall Results. *Bulletin of the Seismological Society of America,* 108 (5A): 2347–2369.

Friedman, J.H. 2001. Greedy function approximation: a gradient boosting machine. *Annals of statistics*: 1189-1232.

Geyin, M. and Maurer, B.W. 2020a. Fragility Functions for Liquefaction-Induced Ground Failure. *Journal of Geotechnical and Geoenvironmental Engineering,* 146(12): 04020142.

Geyin, M. and Maurer, B.W. 2020b. Horizon: CPT-based liquefaction risk assessment and decision software. DesignSafe-CI, doi: 10.17603/ds2-2fky-tm46.

Geyin, M. and Maurer, B.W. 2021a. CPT-Based Liquefaction Case Histories from Global Earthquakes: A Digital Dataset (Version 1). DesignSafe-CI. https://doi.org/10.17603/ds2-wftt-mv37.

Geyin, M. and Maurer, B.W. 2021b. RapidLiq: Software for Near-Real-Time Prediction of Soil Liquefaction. DesignSafe-CI. https://doi.org/10.17603/ds2-4bka-y039.

Geyin, M., Baird, A.J. and Maurer, B.W. 2020. Field assessment of liquefaction prediction models based on geotechnical vs. geospatial data, with lessons for each. *Earthquake Spectra,* 36(3): 1386–1411.

Geyin, M., Maurer, B.W., Bradley, B.A., Green, R.A., and van Ballegooy, S. 2021. CPT-based liquefaction case histories compiled from three earthquakes in Canterbury, New Zealand. Earthquake Spectra: 10.1177/8755293021996367.

Glorot, X. and Yoshua, B. 2010. Understanding the difficulty of training deep feedforward neural networks. Proceedings of the thirteenth international conference on artificial intelligence and statistics: 249–256.

Green, R.A. and Bommer, J.J. 2019. What is the smallest earthquake magnitude that needs to be considered in assessing liquefaction hazard? *Earthquake Spectra,* 35(3): 1441-1464.

Green, R.A., Bommer, J.J., Rodriguez-Marek, A., Maurer, B.W., Stafford, P.J., Edwards, B., Kruiver, P.P., De Lange, G. and Van Elk, J. 2019. Addressing limitations in existing 'simplified' liquefaction triggering evaluation procedures: application to induced seismicity in the Groningen gas field. *Bulletin of Earthquake Engineering,* 17(8): 4539-4557.

Green, R.A., Lasley, S., Carter, M.W., Munsey, J.W., Maurer, B.W., and Tuttle, M.P. 2015. Geotechnical aspects in the epicentral region of the 2011 Mw 5.8 Mineral, Virginia, earthquake. *Geological Society of America, Special Paper 509*: 151-172.

Heath, D.C., Wald, D.J., Worden, C.B., Thompson, E.M., and Smoczyk, G.M. 2020. A global hybrid VS30 map with a topographic slope–based default and regional map insets. *Earthquake Spectra, 36*(3): 1570-1584.

Ho, T.K. 1998. The random subspace method for constructing decision forests. *IEEE Transactions on Pattern Analysis and Machine Intelligence,* 20(8): 832–844.

Holzer, T.L., Noce, T.E., and Bennett, M.J. 2011. Liquefaction probability curves for surficial geologic deposits. *Environmental & Engineering Geoscience, 17*(1): 1-21.

Hopfield, J.J. 1982. Neural networks and physical systems with emergent collective computational abilities. Proc. Natl. Acad. Sci. U.S.A. 79(8): 2554–2558.

Horton, J.D., San Juan, C.A., and Stoeser, D.B. 2017. The State Geologic Map Compilation (SGMC) geodatabase of the conterminous United States (ver. 1.1). *USGS Data Series 1052*, 46 p.

Hutabarat, D. and Bray, J.D. 2021. Effective stress analysis of liquefiable sites to estimate the severity of sediment ejecta. *Journal of Geotechnical and Geoenvironmental Engineering,* 147(5): 04021024.

Idriss, I.M., and Boulanger, R.W. 2008. Soil liquefaction during earthquakes. *Monograph MNO-12* 2008; Earthquake Engineering Research Institute, Oakland, CA, 261 pp.

Iwasaki, T., Tatsuoka, F., Tokida, K., and Yasuda, S. 1978. A practical method for assessing soil liquefaction potential based on case studies at various sites in Japan. *2nd Intl Conf. Microzonation*.

Kaklamanos, J., Bradley, B.; Challenges in Predicting Seismic Site Response with 1D Analyses: Conclusions from 114 KiK-net Vertical Seismometer Arrays. *Bulletin of the Seismological Society of America* 2018;; 108 (5A): 2816–2838. doi: https://doi.org/10.1785/0120180062

Kortum, Z., Liu, K.J., Eberhard, M.O., Berman, J.W., Marafi, N.A., and Maurer, B.W. 2021. Impacts of Cascadia Subduction Zone earthquakes on bridges in Washington State:

SDOF idealized bridges. *Washington State Department of Transportation Research Report 908.1*.

Kramer, S.L. 2008. *Evaluation of Liquefaction Hazards in Washington State, Report No. WA-RD 668.1*, Washington State Transportation Center, Seattle, Washington.

Lehner, B., Verdin, K., and Jarvis, A. 2006. *HydroSHEDS Technical Documentation*. World Wildlife Fund US, Washington, D.C

Lilliefors, H. W. (1967). On the Kolmogorov-Smirnov test for normality with mean and variance unknown. Journal of the American statistical Association, 62(318), 399-402.

Lin, A., Wotherspoon, L., and Motha, J. 2021a. Evaluation of a geospatial liquefaction model using land damage data from the 2016 Kaikoura earthquake. *Bulletin of the New Zealand Society for Earthquake Engineering. In Review.*

Lin, A., Wotherspoon, L., Bradley, B., and Motha, J. 2021b. Evaluation and modification of geospatial liquefaction models using land damage observational data from the 2010–2011 Canterbury Earthquake Sequence. *Engineering Geology*, 287: 106099.

Maurer, B.W., Green, R.A. and Taylor, O.D.S. 2015a. Moving towards an improved index for assessing liquefaction hazard: lessons from historical data. *Soils and Foundations,* 55(4): 778-787.

Maurer, B.W., Green, R.A., Cubrinovski, M., and Bradley, B. 2015b. Assessment of CPT-based methods for liquefaction evaluation in a liquefaction potential index framework. Géotechnique, 65(5): 328-336**.**

Maurer, B.W., Green, R.A., Cubrinovski, M., and Bradley, B.A. 2014. Evaluation of the liquefaction potential index for assessing liquefaction hazard in Christchurch, New Zealand. *Journal of Geotechnical and Geoenvironmental Engineering,* 140(7): 04014032.

MBIE, 2017. Planning and engineering guidance for potentially liquefaction-prone land. New Zealand Ministry of Business, Innovation, and Employment (MBIE), Building System Performance Branch, ISBN 978-1-98-851770-4.

Moss, R.E.S., Seed, R.B., Kayen, R.E., Stewart, J.P., Der Kiureghian, A., and Cetin, K.O. 2006. CPT-based probabilistic and deterministic assessment of in situ seismic soil liquefaction potential. *Journal of Geotechnical and Geoenvironmental Engineering,* 132(8):1032-1051.

NASA, 2020. Distance to nearest coastline. *NASA Ocean Biology Processing Group (OBPG).* < https://oceancolor.gsfc.nasa.gov/docs/distfromcoast/> *last accessed July 2021.*

National Research Council (NRC) 2016. *State of the Art and Practice in the Assessment of Earthquake-Induced Soil Liquefaction and its Consequences*, Committee on Earthquake Induced Soil Liquefaction Assessment (Edward Kavazanjian, Jr., Chair, Jose E. Andrade,

Kandian “Arul” Arulmoli, Brian F. Atwater, John T. Christian, Russell A. Green, Steven L. Kramer, Lelio Mejia, James K. Mitchell, Ellen Rathje, James R. Rice, and Yumie Wang), The National Academies Press, Washington, DC.

Piryonesi, S.M. and El-Diraby, T.E. 2021. Using machine learning to examine impact of type of performance indicator on flexible pavement deterioration modeling. *Journal of Infrastructure Systems,* 27(2): 04021005.

Rashidian, V. and Baise, L.G. 2020. Regional efficacy of a global geospatial liquefaction model. *Engineering Geology*, 105644.

Rashidian, V. and Gillins, D.T. 2018. Modification of the liquefaction potential index to consider the topography in Christchurch, New Zealand. *Engineering Geology,* 232: 68-81.

Rasmussen, C.E. and Williams, C.K.I. 2006. Gaussian Processes for Machine Learning. MIT Press. Cambridge, Massachusetts, 2006.

Robertson, P.K. and Wride, C.E. 1998. Evaluating cyclic liquefaction potential using cone penetration test. *Canadian Geotechnical Journal,* 35(3): 442-459.

Rokach, L. and Maimon, O. 2008. *Data mining with decision trees: theory and applications*. World Scientific Pub Co Inc. ISBN 978-9812771711.

Schmitt, R.G., Tanyas, H., Jessee, M.A.N., Zhu, J., Biegel, K.M., Allstadt, K.E., ... & Knudsen, K.L. 2017a. *An open repository of earthquake-triggered ground-failure inventories* (No. 1064). US Geological Survey.

Schmitt, R.G., Tanyas, H., Jessee, M.A.N., Zhu, J., Biegel, K.M., Allstadt, K.E., ... & Knudsen, K.L. 2017b. *An open repository of earthquake-triggered ground-failure inventories* (ver 2.0, September 2020), US Geological Survey data release collection, accessed Jan 1, 2021, at https://doi.org/10.5066/F7H70DB4.

Shangguan, W., Hengl, T., de Jesus, J.M., Yuan, H., and Dai, Y. 2017. Mapping the global depth to bedrock for land surface modeling. *Journal of Advances in Modeling Earth Systems, 9*(1): 65-88.

USGS 2021. Map of CPT Data. *United States Geological Survey. < https://earthquake.usgs.gov/research/cpt/data/> Accessed July 2021.*

Van Ballegooy, S., Malan, P., Lacrosse, V., Jacka, M.E., Cubrinovski, M., Bray, J.D., O’Rourke, T.D., Crawford, S.A., and Cowan, H. 2014. Assessment of liquefaction-induced land damage for residential Christchurch. *Earthquake Spectra,* 30(1): 31-55.

Vapnik, V. 1995. The Nature of Statistical Learning Theory. Springer, New York.

Wald, D.J. and Allen, T.I. 2007. Topographic slope as a proxy for seismic site conditions and amplification. *Bulletin of the Seismological Society of America,* 97: 1379–1395.

Wald, D.J., Earle, P.S., Allen, T.I., Jaiswal, K., Porter, K., and Hearne, M. 2008. Development of the U.S. Geological Survey's PAGER system (Prompt Assessment of Global Earthquakes for Response). *Proc. 14th World Conf. Earthq. Eng*., Beijing, China, 8 pp.

Wald, D.J., Worden, B.C., Quitoriano, V., and Pankow, K.L. 2005. ShakeMap manual: technical manual, user's guide, and software guide (No. 12-A1).

Wirth, E.A., Frankel, A.D., Marafi, N., Vidale, J.E., and Stephenson, W.J. 2018. Broadband Synthetic Seismograms for Magnitude 9 Earthquakes on the Cascadia Megathrust Based on 3D Simulations and Stochastic Synthetics, Part 2: Rupture Parameters and Variability. *Bulletin of the Seismological Society of America,* 108 (5A): 2370–2388.

Youd, T.L. and Hoose, S.N. 1977. Liquefaction Susceptibility and Geologic Setting. *Proceedings of the Sixth World Conference on Earthquake Engineering* 3, 2189-2194.

Zhu, J., Baise, L.G., and Thompson, E.M. 2017. An updated geospatial liquefaction model for global application. *Bulletin of the Seismological Society of America,* 107(3): 1365-1385.

Zimmaro, P., Nweke, C.C., Hernandez, J.L., Hudson, K.S., Hudson, M.B., Ahdi, S.K., ... and Stewart, J.P. 2020. Liquefaction and related ground failure from July 2019 Ridgecrest earthquake sequence. *Bulletin of the Seismological Society of America, 110*(4): 1549-1566.

Ziotopoulou, K. and Boulanger, R.W. 2016. Plasticity modeling of liquefaction effects under sloping ground and irregular cyclic loading conditions. *Soil Dynamics and Earthquake Eng,* 84: 269-283.

APPENDIX A: *RAPIDLIQ* USER MANUAL

***RapidLiq* User Manual**
v.1.0.

A.1 Summary

RapidLiq is a Windows software program for predicting liquefaction-induced ground failure using geospatial models, which are particularly suited for regional scale applications such as (i) loss estimation and disaster simulation; (ii) city planning and policy development; (iii) emergency response; and (d) post-event reconnaissance (e.g., to remotely identify sites of interest). *RapidLiq* v1.0 includes four such models. One is a logistic regression model developed by Rashidian and Baise (2020) that has been adopted into United States Geological Survey (USGS) post-earthquake data products but that is not often implemented by individuals because of the geospatial variables that must be compiled. The other three models are the machine and deep learning models developed in this report. All necessary predictor variables are compiled within *RapidLiq*, making user implementation trivial. The only required input is a ground motion raster easily downloaded within minutes of an earthquake, or available for enumerable future earthquake scenarios. This gives the software near-real-time capabilities, such that ground failure can be predicted at regional scale within minutes of an earthquake. The software outputs geotiff files mapping the probabilities of liquefaction-induced ground failure. These files may be viewed within the software or explored in greater detail using GIS or one of many free geotiff web explorers (e.g., http://app.geotiff.io/). The software also allows for tabular input, should a user wish to enter specific sites of interest and ground-motion parameters at those sites, rather than

study the regional effects of an earthquake. *RapidLiq* v.1.0 operates in the contiguous U.S. and completes predictions within 10 seconds for most events.

A.2 Installation and Running *RapidLiq*

Install *RapidLiq* using "RapidLiqv1_Installer.exe." If prompted to do so, extract all zipped contents prior to continuing the installation. In addition, you may be warned by the Windows OS that .exe files from unknown sources could be harmful. Please ignore any such message and click "run anyway." There are no specific system requirements. Four GB of RAM will be enough for most scenarios, but if high resolution rasters with a large land domain will be used (2 million + pixels), at least 8 GB of RAM is recommended. Please note that the software will initiate slowly the first time it is used, since some of the installation process occurs during first use of the software. The software will thereafter open more quickly.

A.3 Using RapidLiq

The *RapidLiq* user interface has two main tabs that perform the same analyses with different types of inputs. Both use a simple three-step process wherein (1) an input file is loaded; (2) model parameters are extracted; and (3) analyses are performed.

The first tab (Raster) requires a raster file in either .xml (Extensible Markup Language) or .tif (GeoTagged Image File) format. This option is best for studying the regional effects of an earthquake. The first format can be downloaded from the USGS earthquake catalog (https://earthquake.usgs.gov/earthquakes/search/) minutes after an event, or from the USGS scenario catalog (https://earthquake.usgs.gov/scenarios/catalog/) for future scenario events. The second format (.tiff) is a more general, flexible format, allowing for motions from various sources to be analyzed. In either case, the software extracts predictor variables across the ShakeMap extents and outputs geotiff files mapping the probabilities of liquefaction-induced ground failure. These output files (saved in the same directory as the input file) may be viewed within the software or explored in greater detail using GIS or one of many free geotiff web explorers (e.g., http://app.geotiff.io/).

The second tab (tabular) allows for tabular input, should a user wish to enter specific sites of interest and ground-motion parameters at those sites, rather than study the regional effects of an earthquake. With this option, an .xlsx input file is required with the following ordered columns: (1) Latitude (WGS84); (2) Longitude (WGS84); (3) Moment Magnitude (*Mw*); (4) Peak Ground Acceleration, *PGA*, in g; and (5) Peak Ground Velocity, *PGV*, in cm/sec. With this

option, the software creates an .xlsx output file within the same directory where the input file is located.

Use of the software is next demonstrated via two examples.

A.3.1 Example 1. Input Type: .xml Raster

Extensible Markup Language (.xml) ground motion rasters are available from the USGS for past earthquakes (https://earthquake.usgs.gov/earthquakes/search/) and future scenario events (https://earthquake.usgs.gov/scenarios/catalog/). These files contain all necessary seismic data, including earthquake magnitude and the regional distribution of shaking intensities. Once on an event page, navigate to the event's "ShakeMap."

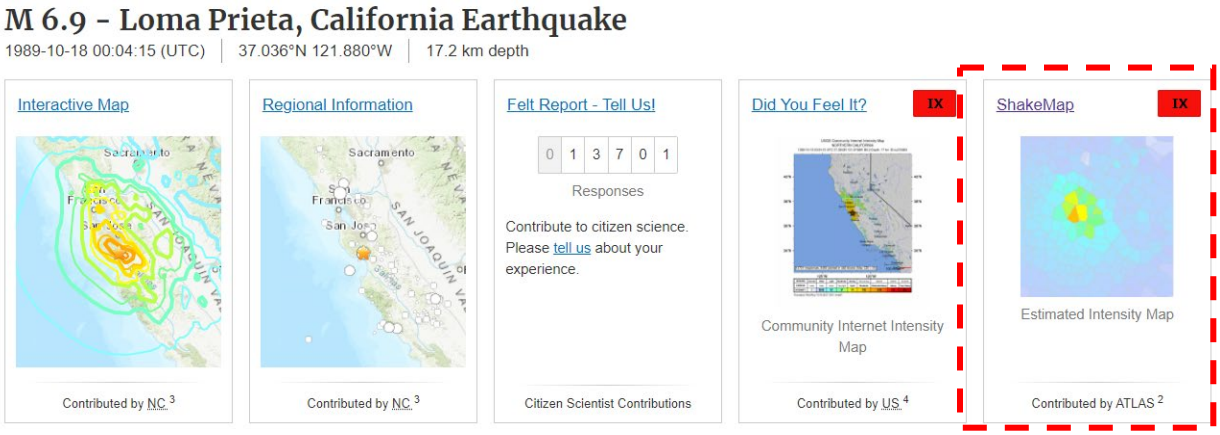

Figure A.1 Navigating to ShakeMaps within the USGS event catalogs

Next, below the map of ShakeMap information, select "Downloads."

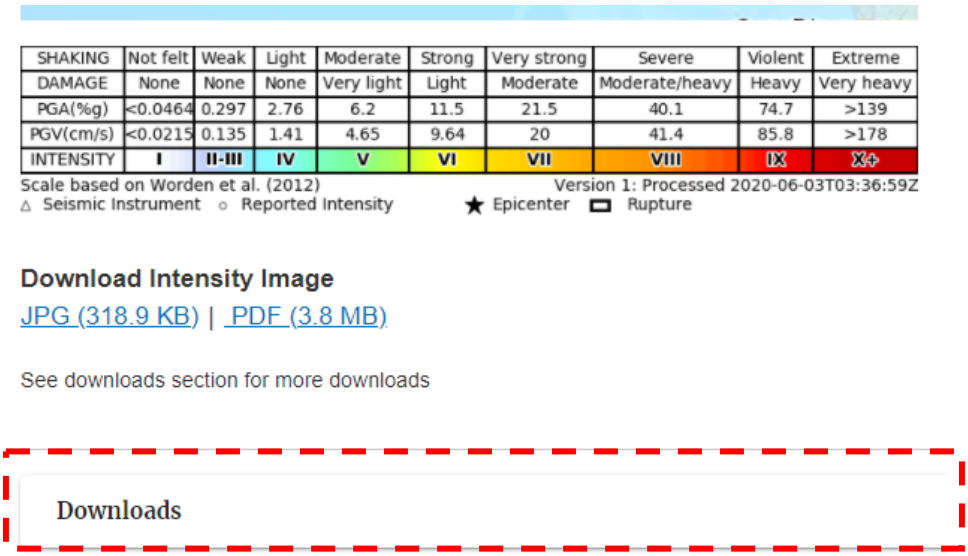

Figure A.2 Select the Downloads dropdown menu within a given ShakeMap

From the dropdown menu, a multitude of download options will appear. The exact position and title of the .xml file may change with time. For the 1989 Loma Prieta earthquake, for example, it appears as shown in figure A.3.

Figure A.3 Location and name of XML grid file for 1989 Loma Prieta, California, earthquake

For the 2020 Stanley, Idaho earthquake, it appears as shown in figure A.4.

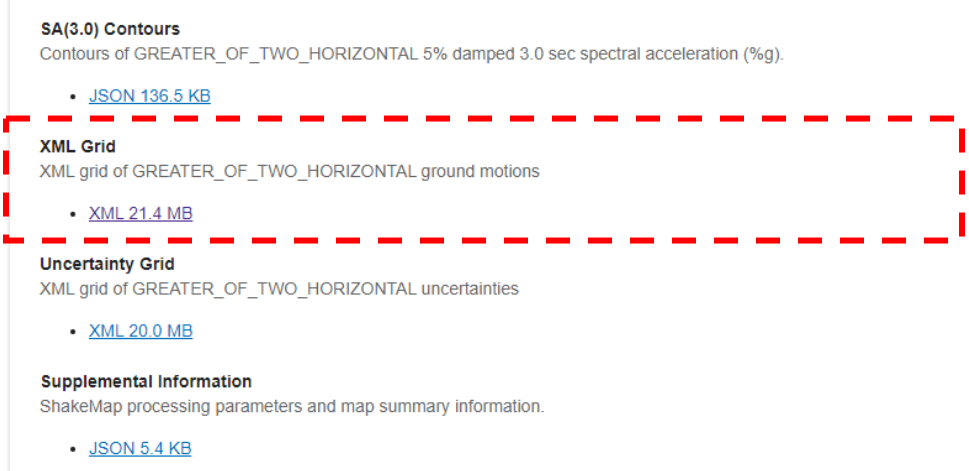

Figure A.4 Location and name of XML grid file for 2020 Stanley, Idaho, earthquake

Open and save the .xml file to any desired file directory. Please note that an "OutFiles" subfolder will be created in the same directory. Here, the program outputs will be saved.

In *RapidLiq*, under the "Raster" tab, select the "Input ShakeMap" button. Specify the input type as .xml and direct *RapidLiq* to the .xml file of your choosing. Please wait several seconds as the file is loaded. *RapidLiq* will inform the user whether the input was successful. Press OK to continue.

An interactive map of the *PGA* raster with a scalebar will appear on the screen, as shown in figure A.5.

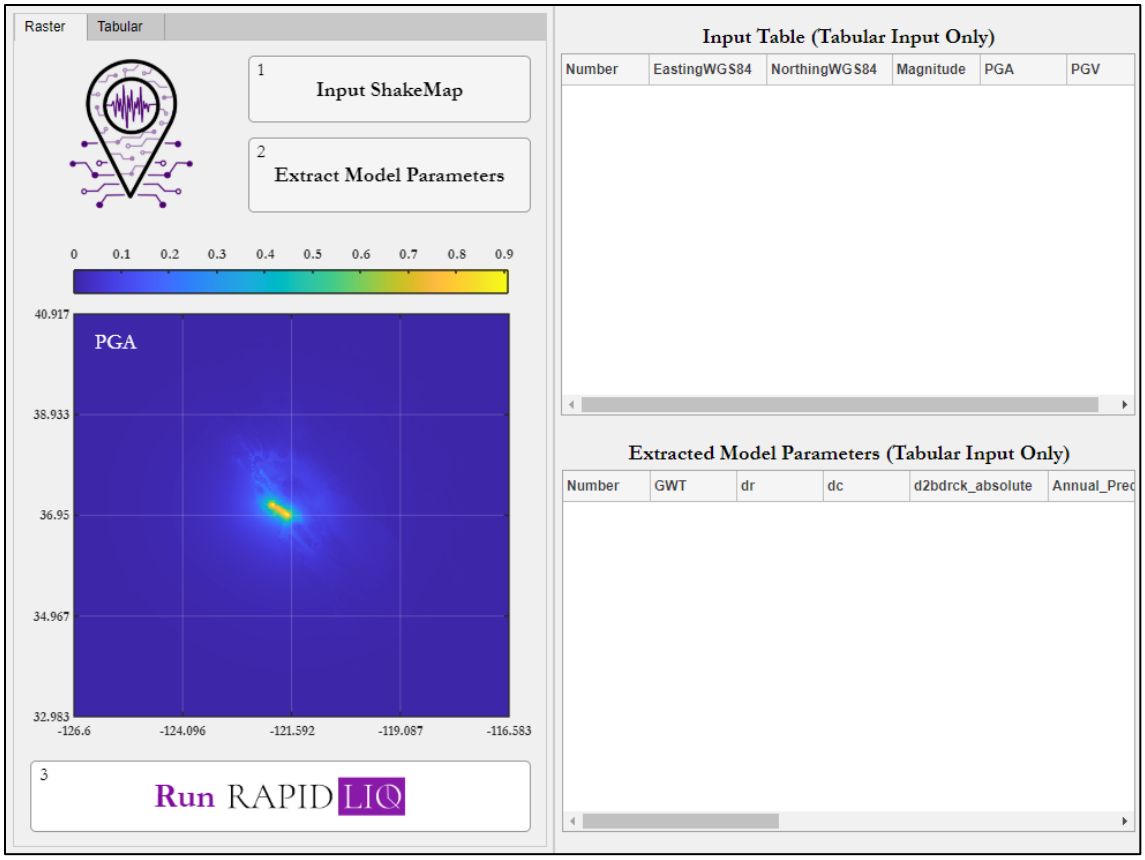

Figure A.5 RapidLiq interface after Raster input

Next, select the "Extract Model Parameters" button to gather all model variables over the ShakeMap extents. In *RapidLiq* v1.0, these include predicted V_{S30} (Heath et al., 2020); predicted ground water depth (Fan and Miguez-Macho, 2020); measured distance to river (Lehner et al., 2006) and measured distance to coast (NASA, 2012); predicted depth to bedrock (Shangguan et al. 2017); measured annual precipitation (Fick and Hijmans, 2017); and the predicted (binomial) presence of unconsolidated soil, sandy soil, clayey soil, and silty soil, as obtained from the USGS National Geologic Map compilation (Horton et al. 2017).

Please wait several seconds until extraction is complete. After the process finishes, a pop-up window should inform the user whether the parameter extraction was successful. Press OK to continue. To compute predictions of liquefaction-induced ground failure using all available models, select the "Run *RapidLiq*" button. Rapidliq v.1.0 contains four models. These include the logistic regression model of Rashidian and Baise (2020) and the deep learning (DL), machine

learning (ML), and Ensemble (ENS) models proposed by Geyin et al. (2021). All four models are described in detail by Geyin et al. (2021).

All calculations should be performed within several seconds After the predictions are made, a window informs the user whether the calculation process was successful. Press OK to plot the model predictions on the screen, as shown in figure A.6. Results from each model, by default, are also saved to the aforementioned "OutFiles" folder as separate geotiff (.tiff) files.

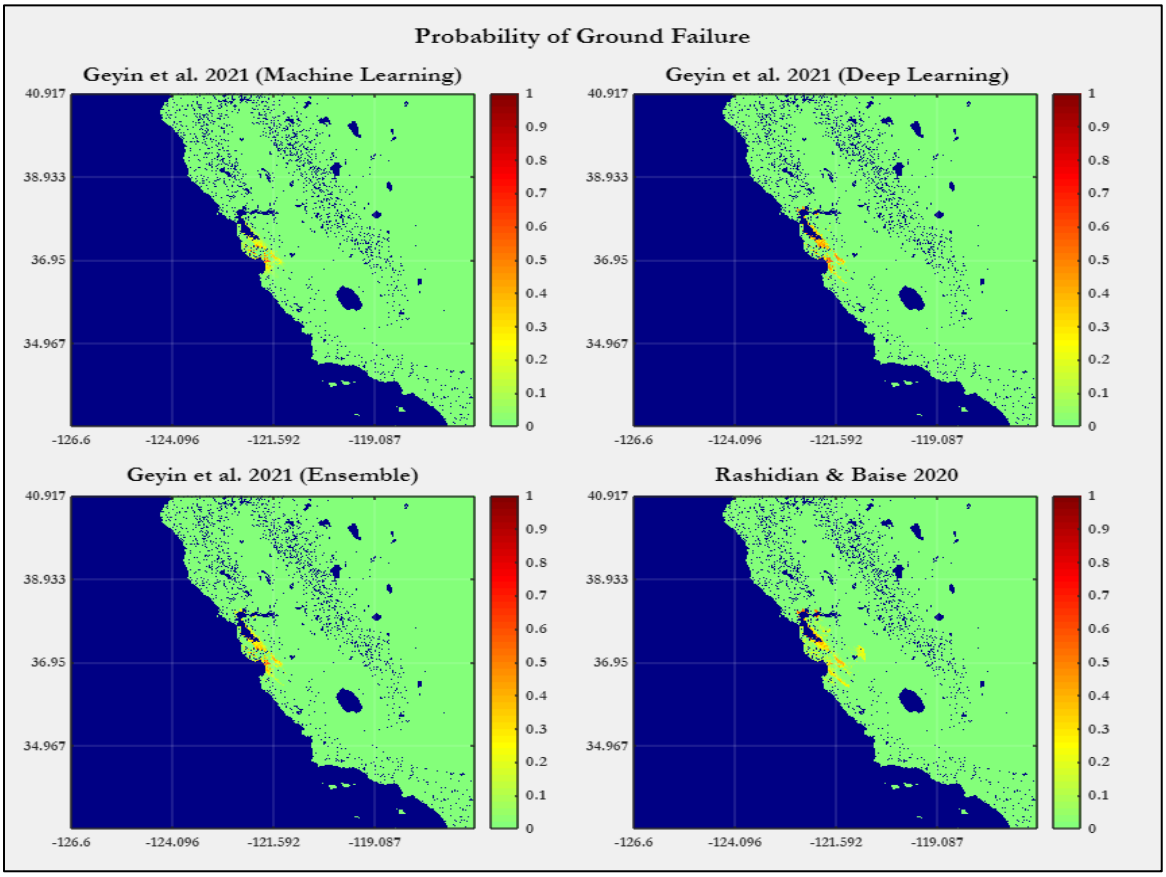

Figure A.6 RapidLiq output from all 4 models

To explore the outputs in greater detail (e.g., to make custom maps, or to further explore and study the predictions), the output files are easily opened in GIS or one of many free geotiff web explorers (e.g., http://app.geotiff.io/). As an example, results for the 2011 Mineral, Virginia, earthquake are shown in figure A.7 as produced by the geotiff.io web explorer, which has several simple statistical analysis tools built in.

Alternatively, but following a very similar process, *RapidLiq* allows for geotiff (.tiff) input files, which might be obtained from various sources (e.g., ground motion simulations). Using this approach, .tiff files containing *PGA* and *PGV* are separately input, and the earthquake magnitude is entered in a text window.

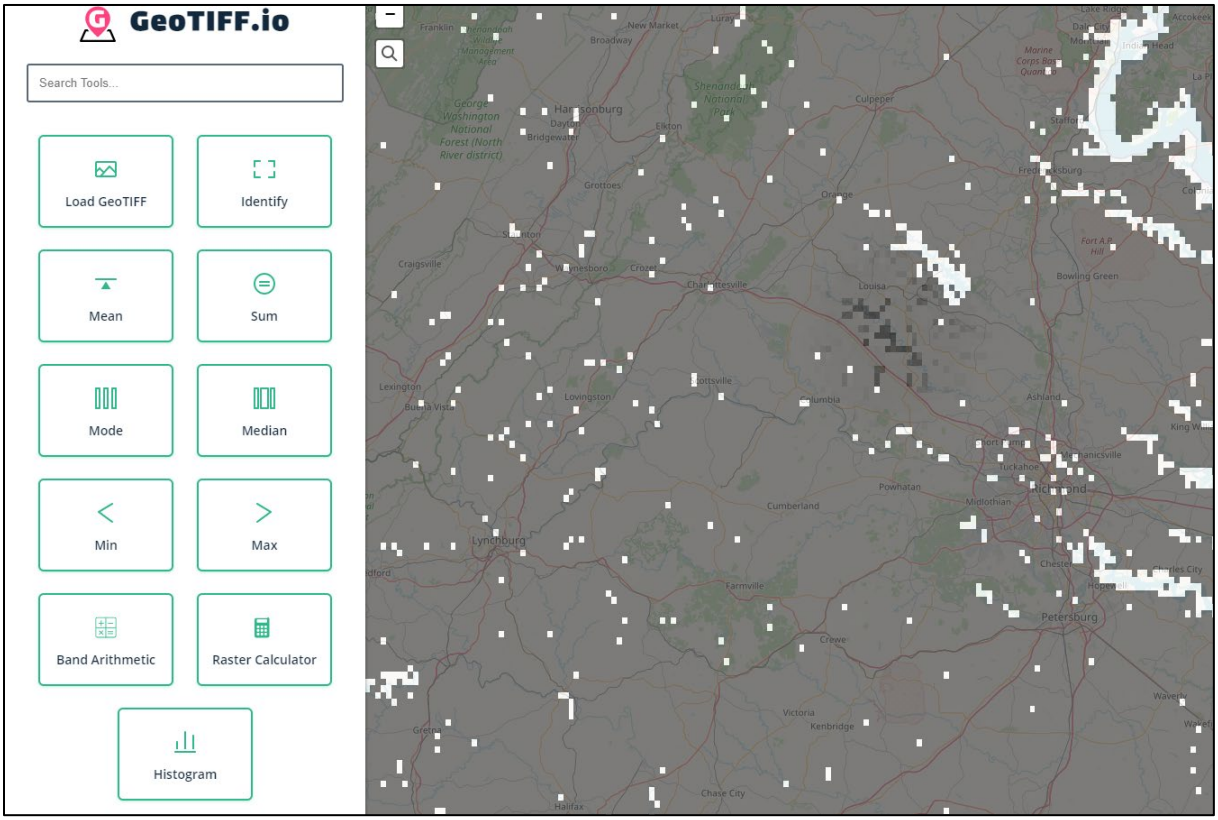

Figure A.7 Exploring RapidLiq predictions with the http://app.geotiff.io/) web explorer

A.3.2. Example 2. Input type: Tabular

The software also allows for tabular input, should a user wish to enter specific sites of interest and ground-motion parameters at those sites, rather than study the regional effects of an earthquake. To use this option, select the "Tabular" tab from the user interface and create an .xlsx file with columnar data in the order of (1) Latitude (WGS84); (2) Longitude (WGS84); (3) Moment Magnitude (*Mw*); (4) Peak Ground Acceleration, *PGA*, in g; and (5) Peak Ground Velocity, *PGV*, in cm/sec. An example input file is shown in Figure A.8. Import this table to *RapidLiq* by selecting the "Input Table" button. *RapidLiq* will inform the user whether the import is successful and display the tabular data on the upper right side of the user interface.

Next, select the “Extract Model Parameters” button to compile necessary model inputs. This may take several seconds depending on the size of the dataset. After extraction is complete, parameters at each site of interest are displayed on the lower right side of the user interface. Press “Run *RapidLiq*” to compute the predictions using each of the four models. A table of results will appear, and a new timestamped .xlsx file will be created in the directory where the input file is located.

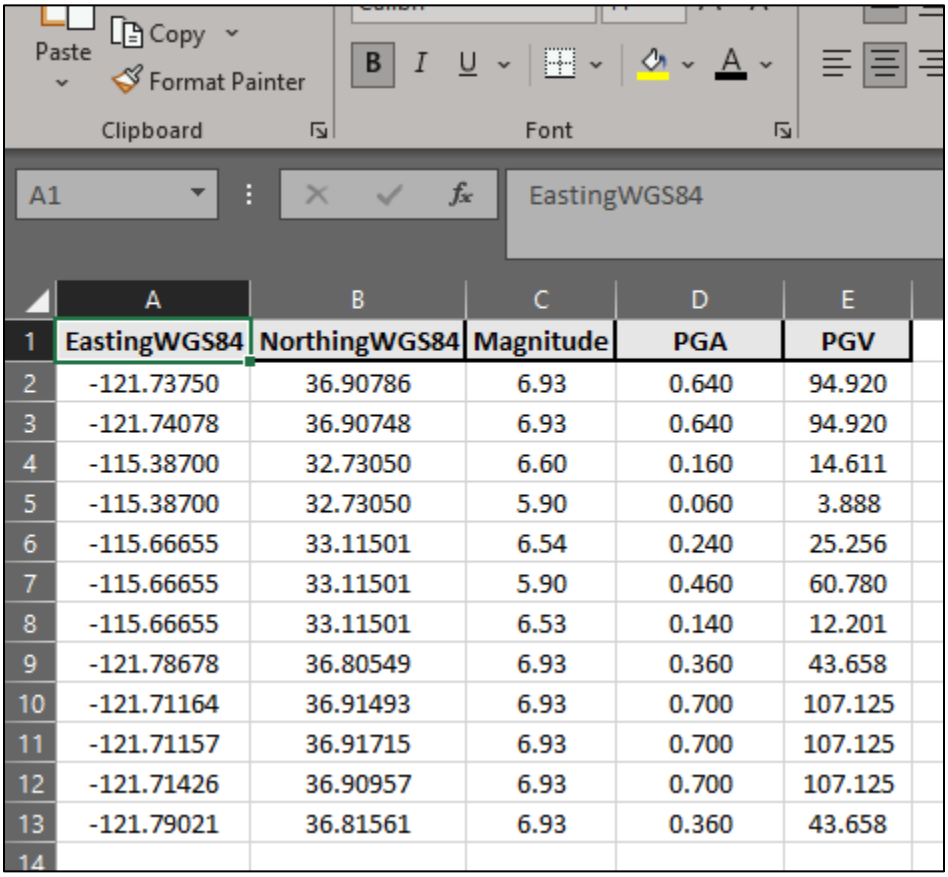

	A	B	C	D	E
1	EastingWGS84	NorthingWGS84	Magnitude	PGA	PGV
2	-121.73750	36.90786	6.93	0.640	94.920
3	-121.74078	36.90748	6.93	0.640	94.920
4	-115.38700	32.73050	6.60	0.160	14.611
5	-115.38700	32.73050	5.90	0.060	3.888
6	-115.66655	33.11501	6.54	0.240	25.256
7	-115.66655	33.11501	5.90	0.460	60.780
8	-115.66655	33.11501	6.53	0.140	12.201
9	-121.78678	36.80549	6.93	0.360	43.658
10	-121.71164	36.91493	6.93	0.700	107.125
11	-121.71157	36.91715	6.93	0.700	107.125
12	-121.71426	36.90957	6.93	0.700	107.125
13	-121.79021	36.81561	6.93	0.360	43.658
14					

Figure A.8 Example input table for RapidLiq tabular analyses